Development and validation of an orthotropic 3D elasto-plastic damage model for wood, considering fiber deviations

Seeber, Franziska; Khaloian-Sarnaghi, Ani; Yu, Taoyi; Duddeck, Fabian; van de Kuilen, Jan Willem

DOI
10.1016/j.engstruct.2024.117928

Publication date
2024

Document Version
Final published version

Published in
Engineering Structures

Engineering Structures 308 (2024) 117928

Contents lists available at ScienceDirect

Engineering Structures

journal homepage: www.elsevier.com/locate/engstruct

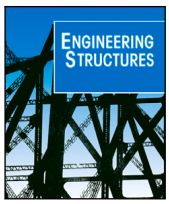

Development and validation of an orthotropic 3D elasto-plastic damage model for wood, considering fiber deviations

Franziska Seeber [a,*], Ani Khaloian-Sarnaghi [a], Taoyi Yu [a], Fabian Duddeck [a], Jan-Willem van de Kuilen [a,b]

[a] Technical University of Munich, TUM School of Engineering and Design, Arcisstr. 21, Munich 80333, Germany
[b] Delft University of Technology, Faculty of Civil Engineering and Geosciences, Biobased Structures and Materials, Stevinweg 1, Delft 2628 CN, Netherlands

ARTICLE INFO

Keywords:
3D orthotropic materials
Elasto-plastic CDM
Experimental clear wood validation
Fiber deviations
Heterogeneity
Failure modes

ABSTRACT

This contribution aims for an enhanced numerical representation for strength prediction of timber. This implies a validated elasto-plastic continuum damage model which considers orthotropy and heterogeneity of the material, and represents the ductile behavior under compression and the brittle material behavior under tension dependent on the three-dimensional orthogonal fiber directions. The behavior under compression is captured by Hill (1948) plasticity and an exponential hardening law enhanced by the loading direction dependency. The same model covers also the brittle damaging behavior by means of continuum damage mechanics (CDM). In this study, a separated damage mode (SDM) criterion with simultaneously evolving damage variables is investigated. After the experimental validation of the model for axially loaded clear wood samples, the developed numerical model is implemented to a sawn timber with fiber deviation, where homogenization of the material and simplification to transverse isotropy is not anymore possible. The 3D orthotropic material behavior is experimentally validated for this application example with bi-axial loading and aims for further numerical investigation of wood with heterogeneities as occurring in sawn (hard)wood for its efficient use in engineered wood products such as glued laminated timber.

1. Introduction

Numerical simulations allow us to describe the mechanical/material behavior of a structural component when containing relevant constitutive material laws. For wood, this means to incorporate linear and nonlinear material laws for the elastic, plastic, damaging, moisture- and time-dependent behavior and to combine them in a model for the prediction of the elastic and post-elastic material behavior until failure. Stress and strain fields can be predicted numerically and can be obtained at different scales, including micro-, meso- and macro-scale of the naturally grown fiber composite wood. Since different wood species have different micro-structural characteristics, the goal is to develop and validate a generally applicable material model at macro-scale with material input parameters that can be varied accordingly for the wood species.

European beech (*Fagus Sylvatica* L.) is considered in this study to develop the numerical model and to validate the results. Throughout the last decades, the share of beech has increased in European forests. For the use of beech wood in construction purposes, its complex anatomic structure, including fiber deviations and irregularly occurring heterogeneities such as knots and strong variations of the pith location along the boards [1] need to be investigated to understand their influence on mechanical properties such as strength. This knowledge can then be used in the development of engineered wood products. The production of beech glued laminated timber (GLT) is relatively scarce at present. However, high-grade GLT beams demonstrate the potential through the targeted combination of low-grade and high-grade lamella qualities [2]. Essential for optimized GLT beams is the numerical investigation of such "low-grade" wood components with appropriate constitutive material laws for including elasticity, plasticity, brittle/ductile failure as well as moisture-, temperature and time dependent behaviors [3].

The elastic material range is substantially affected by the orthotropic material orientation, which is mostly introduced by means of tensor transformation according to the fiber orientation from the grain flow analysis around knots [4,5], laser scanning information [6,7] or CT-scanning information [8].

The post-elastic range for wood is strongly dependent on the load direction. For compressive stresses, the behavior is quasi-ductile and can be represented by plasticity. Several single surface plasticity models [9,10] were extended to multi-surface plasticity models [11–13] to

* Corresponding author.
E-mail address: seeber@hfm.tum.de (F. Seeber).

https://doi.org/10.1016/j.engstruct.2024.117928
Received 5 December 2023; Received in revised form 22 February 2024; Accepted 24 March 2024
Available online 6 April 2024

be able to describe the post-elastic material behavior in a more accurate way.

For tensile or shear stresses, brittle softening and brittle failure can be represented by different methods. Continuum Damage Mechanics (CDM) introduces the effective stress concept [14]: After a defined stress state is reached, damage initiates and evolves following the defined damage evolution law to evoke the weakening of the material due to the occurrence of micro-cracks. Micro-cracks consequently accumulate to a macro-crack and lead to failure. This concept is mainly established for composites [15,16] and adapted to wood [17]. Different damage initiation criteria such as the ones provided in [9,10,18–20] can be included. Other methods than CDM, are e.g. based on fracture mechanics, with the focus on discontinuous crack propagation such as cohesive zone models [21], XFEM approaches [22,23], and lately also phase field models [24,25].

Different approaches already combine both post-elastic ductile and brittle material behaviors in one model with the purpose to analyze wood e.g. in connections and investigate the effect of different parameters on the load carrying capacity and failure behavior in a cost-efficient way [17,26–28]. Models are established either with a multi-linear approach in [29] or with nonlinear material laws. The latter ones focus on elasto-plastic damage model for transversely isotropic material in 3D [30,31] or for plane stress situation in 2D in [23,32]. Their main motivation is on describing dowel-type connections with the ductile embedding failure as well as the brittle cracking of wood considering different failure initiation criteria.

Besides investigations on connections, the strength of sawn wooden components such as beech boards strongly depends on heterogeneities as fiber deviations at different local positions. In this case different bi-axial loading situations can occur and need to be analyzed. Bi-axial loading situations are analyzed experimentally e.g. in [33,34] for clear wood and represented numerically in models based on plasticity [11,12] or in general polynomial stress criteria in [35] and its comparison in [20]. In addition, combined loading is studied specifically for the combination of shear and compression e.g. in [36–38].

Previous models had a look at multiple of criteria to cover the complex mechanical behavior of wood. However such models need to be validated and further developed to cover the comprehensive 3D nonlinear material response, which considers plasticity and damage for different loading configurations under directional changes of fibers. The model in this study aims to prevent homogenization of the material by considering local variation of the properties. It further includes the validation of the developed 3D nonlinear material model and specially shows its application for cases with locally varying bi-axial 3D stress configurations. The objective of this contribution is an enhanced and validated representation of the post-elastic nonlinear three-dimensional orthotropic behavior in a three-dimensional orthotropic material by means of an elasto-plastic damage model. The goal is to predict different failure modes as a consequence of damage evolving in different directions due to local stress concentrations (or stress interactions) in a parallel to the fiber tensile tested sawn board with fiber deviation. Additionally, the necessary representation of direction-dependent plasticity for the orthotropic material behavior of wood is incorporated considering hardening in the different directions. Can an elasto-plastic damage model contribute to understanding local resistance (in e.g. beech wood) with strong fiber deviation for predicting the strength of sawn timber?

Different failure behavior is incorporated for tension and compression, including ductile plasticity in Section 2.1 considering hardening in the different directions and different damage initiation criteria in Section 2.2. The model is validated for the orthotropic direction dependency for uni-axial tests under compression (Section 4.1) and tension (Section 4.2). Accordingly, a separate mode damage criterion is developed in this study for describing the material with local fiber deviations. Finally, these failure criteria are applied on a board loaded in tension with 3D fiber deviation and its according representation of strength and failure mode in Section 4.3.

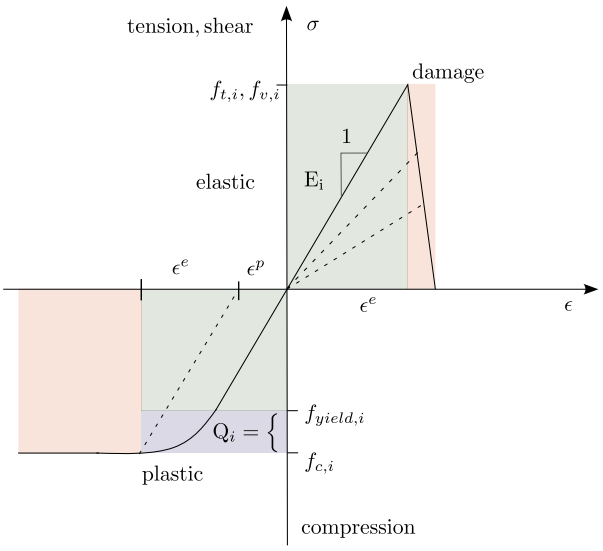

Fig. 1. Schematic material behavior dependent on the orthotropic directions i as well as on the loading direction.

2. Constitutive nonlinear elasto-plastic damage model

The mechanical behavior of wood is characterized by a strong orthogonal directional- and stress-sign dependency due to its natural fiber structure. L represents the longitudinal fiber direction, R the radial direction and T the tangential direction in the following sections. This will be represented in the following constitutive model by three elastic moduli (tensile and compression moduli are assumed to be the same), three shear moduli, and six Poisson ratios in the elastic range. The post-elastic material behavior is further described by nine different strength values dependent on direction and stress-sign (compression, tension or shear). Consequently, the definition of the different material behavior results in different failure modes, which were investigated on a micro-mechanical level inter alia in [39], shall be subdivided at meso-/macro-scale to four principle patterns [11]. Brittle damage due to tensile or shear stresses leads to micro-cracks in the material which accumulate and form a macro-crack. *Fiber rupture* (parallel to fiber direction) and *inter-fiber band shear failure* (in radial or tangential direction) are the consequence. Ductile plasticity due to compressive stress leads to high deformations while maintaining toughness. This mechanical behavior is driven by *cell wall buckling* (parallel to fiber direction) and *fiber cell crushing* (in radial or tangential direction), which further leads to densification at large strains.

In the following, a nonlinear three-dimensional elasto-plastic damaging material model is presented to capture the described material behavior. As visualized in Fig. 1, it consists of independent post-elastic parts (ductile plasticity and brittle softening) which represent the material behavior in accordance with [40,41]. Ductile plasticity in Section 2.1 is based on [42] and covers an anisotropic yield surface $f_{yield,i}$. Together with a nonlinear isotropic hardening law q_i, the model takes into consideration the plastic material behavior and the compressive material strength $f_{c,i}$, dependent on the decisive loading direction (purple region in Fig. 1). Brittle damage in Section 2.2 is modeled by CDM [14]. The reduction of the elastic stiffness in different material directions (including normal and shear stresses) can occur simultaneously, which reflects on combined loading situations.

In addition in this section an overview is going to be given about the already existing damage initiation criteria. Once damage is initiated, it results in a damage vector taking the direction dependency and the consequent failure mode into account.

In the elastic range, Hooke's law is applied:

$$\hat{\boldsymbol{\sigma}} = \mathbf{C}_0 \cdot \boldsymbol{\varepsilon}^{\mathrm{e}},$$
$$\boldsymbol{\sigma} = \mathbf{C}_{\mathrm{d}} \cdot \boldsymbol{\varepsilon}^{\mathrm{e}}. \tag{1}$$

where $\hat{\boldsymbol{\sigma}}$ is the effective stress acting only on the elastic, non-damaged material according to CDM [14]. $\mathbf{C}_0$ is the initial undamaged orthotropic stiffness tensor. The stress $\boldsymbol{\sigma}$ in a damaged state can be calculated using the damaged orthotropic stiffness tensor $\mathbf{C}_{\mathrm{d}}$.

The strain vector $\boldsymbol{\varepsilon}$ is composed of an elastic part $\boldsymbol{\varepsilon}^{\mathrm{e}}$ and a plastic part $\boldsymbol{\varepsilon}^{\mathrm{p}}$:

$$\boldsymbol{\varepsilon} = \boldsymbol{\varepsilon}^{\mathrm{e}} + \boldsymbol{\varepsilon}^{\mathrm{p}}. \tag{2}$$

Consequently, the stress tensors can be computed as:

$$\hat{\boldsymbol{\sigma}} = \mathbf{C}_0 \cdot (\boldsymbol{\varepsilon} - \boldsymbol{\varepsilon}^{\mathrm{p}}),$$
$$\boldsymbol{\sigma} = \mathbf{C}_{\mathrm{d}} \cdot (\boldsymbol{\varepsilon} - \boldsymbol{\varepsilon}^{\mathrm{p}}). \tag{3}$$

2.1. Ductile plasticity (compression and shear)

The single surface failure criterion according to Hill (1948) [9] is considered for initiating plasticity under compression and shear. Since wood presents a brittle behavior under tension, this criterion is not used for modeling of tensile cases. It is a quadratic criterion for describing anisotropic plastic deformations and it is modified here to consider the decisive loading-stress in the current stress situation (in compression and shear).

The anisotropic Hill (1948) criterion in its initial form is

$$F(\sigma_{11}-\sigma_{33})^2 + G(\sigma_{33}-\sigma_{11})^2 + H(\sigma_{11}-\sigma_{22})^2 + 2L\sigma_{23}^2 + 2M\sigma_{31}^2 + 2N\sigma_{12}^2 = 1, \tag{4}$$

where the material parameters F, G, H, L, M, N are dependent on the compression strength $f_{\mathrm{c},j}$ and shear strength $f_{\mathrm{v},jk}$, $j,k = \mathrm{L},\mathrm{R},\mathrm{T}$:

$$F = \frac{1}{2}\left(\frac{1}{f_{\mathrm{c,R}}^2} + \frac{1}{f_{\mathrm{c,T}}^2} - \frac{1}{f_{\mathrm{c,L}}^2}\right), L = \frac{1}{2f_{\mathrm{v,RT}}^2},$$
$$G = \frac{1}{2}\left(\frac{1}{f_{\mathrm{c,T}}^2} + \frac{1}{f_{\mathrm{c,L}}^2} - \frac{1}{f_{\mathrm{c,R}}^2}\right), M = \frac{1}{2f_{\mathrm{v,LT}}^2}, \tag{5}$$
$$H = \frac{1}{2}\left(\frac{1}{f_{\mathrm{c,L}}^2} + \frac{1}{f_{\mathrm{c,R}}^2} - \frac{1}{f_{\mathrm{c,T}}^2}\right), N = \frac{1}{2f_{\mathrm{v,LR}}^2}.$$

The Hill criterion can further be written in the following matrix form

$$f(\boldsymbol{\sigma}) = \boldsymbol{\sigma}^{\mathrm{T}} : \mathbf{A} : \boldsymbol{\sigma} - 1, \tag{6}$$

with

$$\mathbf{A} = \begin{bmatrix} (H+G) & -H & -G & 0 & 0 & 0 \\ -H & (F+H) & -F & 0 & 0 & 0 \\ -G & -F & (F+G) & 0 & 0 & 0 \\ 0 & 0 & 0 & 2N & 0 & 0 \\ 0 & 0 & 0 & 0 & 2M & 0 \\ 0 & 0 & 0 & 0 & 0 & 2L \end{bmatrix}. \tag{7}$$

Since the plastic material behavior for wood is restricted to compressive normal stresses and strongly depends on the orthogonal direction, the Hill (1948) plasticity criterion [9] is enhanced in this paper for taking the actual loading status into consideration. After determining the decisive loading situation, the modification is performed in all directions. This process is given in Eqs. (8)–(13). It is similar to [30], where only one loading situation was considered for $\mathbf{A}$ and hence lacks in capturing the orthotropic material responses.

According to the current stress situation, the yield function in Eq. (6) is extended to isotropic hardening as:

$$f(\boldsymbol{\sigma}, q_i) = \boldsymbol{\sigma}^{\mathrm{T}} : \mathbf{A} : \boldsymbol{\sigma} - \frac{(f_{\mathrm{y},i} + q_i)^2}{f_{\mathrm{c},i}^2}, \tag{8}$$

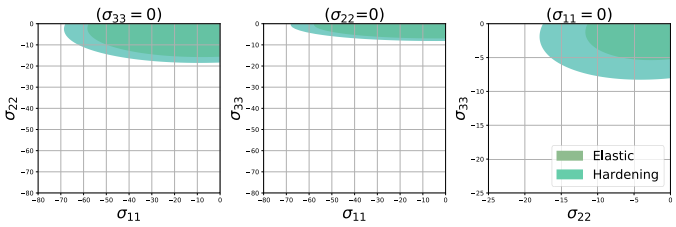

Fig. 2. 2D failure surfaces of the adapted Hill criterion [9], for which the strength and hardening variables are listed in Table 1.

where the strength in the decisive direction is $f_{\mathrm{c},i}^2 = (f_{\mathrm{y},i} + q_i)^2$ with i being the determined decisive loading direction following Eq. (9), $f_{\mathrm{y},i}$ representing the yield strength in the same direction and q_i representing the hardening law (Eq. (12)):

$$\begin{aligned}
&\text{if} \quad \frac{|\sigma_{11}|}{f_{\mathrm{c,L}}} \geq \frac{|\sigma_{22}|}{f_{\mathrm{c,R}}} \quad \text{and} \quad \frac{|\sigma_{11}|}{f_{\mathrm{c,L}}} \geq \frac{|\sigma_{33}|}{f_{\mathrm{c,T}}} \quad : \quad f_{\mathrm{c},i} = f_{\mathrm{c,L}}, \\
&\text{if} \quad \frac{|\sigma_{22}|}{f_{\mathrm{c,R}}} \geq \frac{|\sigma_{11}|}{f_{\mathrm{c,L}}} \quad \text{and} \quad \frac{|\sigma_{22}|}{f_{\mathrm{c,R}}} \geq \frac{|\sigma_{33}|}{f_{\mathrm{c,T}}} \quad : \quad f_{\mathrm{c},i} = f_{\mathrm{c,R}}, \\
&\text{if} \quad \frac{|\sigma_{33}|}{f_{\mathrm{c,T}}} \geq \frac{|\sigma_{11}|}{f_{\mathrm{c,L}}} \quad \text{and} \quad \frac{|\sigma_{33}|}{f_{\mathrm{c,T}}} \geq \frac{|\sigma_{22}|}{f_{\mathrm{c,R}}} \quad : \quad f_{\mathrm{c},i} = f_{\mathrm{c,T}}.
\end{aligned} \tag{9}$$

Consequently the anisotropic Hill-yield criterion is adapted and Eq. (8) can be restructured to

$$f(\boldsymbol{\sigma}, q_i) = \quad = \sqrt{\boldsymbol{\sigma}^{\mathrm{T}} : \tilde{\mathbf{A}} : \boldsymbol{\sigma}} - (f_{\mathrm{y},i} + q_i). \tag{10}$$

Due to the adaption of the Hill-matrix $\tilde{\mathbf{A}}$, the material parameters F, G, H of Hill-plasticity are reformulated to

$$\tilde{F} = \frac{1}{2}\left(\frac{1}{f_{\mathrm{c,R}}^2/f_{\mathrm{c},i}^2} + \frac{1}{f_{\mathrm{c,T}}^2/f_{\mathrm{c},i}^2} - \frac{1}{f_{\mathrm{c,L}}^2/f_{\mathrm{c},i}^2}\right),$$
$$\tilde{G} = \frac{1}{2}\left(\frac{1}{f_{\mathrm{c,T}}^2/f_{\mathrm{c},i}^2} + \frac{1}{f_{\mathrm{c,L}}^2/f_{\mathrm{c},i}^2} - \frac{1}{f_{\mathrm{c,R}}^2/f_{\mathrm{c},i}^2}\right),$$
$$\tilde{H} = \frac{1}{2}\left(\frac{1}{f_{\mathrm{c,L}}^2/f_{\mathrm{c},i}^2} + \frac{1}{f_{\mathrm{c,R}}^2/f_{\mathrm{c},i}^2} - \frac{1}{f_{\mathrm{c,T}}^2/f_{\mathrm{c},i}^2}\right), \tag{11}$$
$$\tilde{L} = \frac{1}{2f_{\mathrm{RT}}^2/f_{\mathrm{c},i}^2}, \tilde{M} = \frac{1}{2f_{\mathrm{LT}}^2/f_{\mathrm{c},i}^2}, \tilde{N} = \frac{1}{2f_{\mathrm{LR}}^2/f_{\mathrm{c},i}^2}.$$

The failure surfaces and the isotropic hardening surfaces are visualized in 2D in Fig. 2. The hardening law q_i can be expressed using the hardening variable α_i:

$$q_i = K(\alpha_i) \tag{12}$$

with the exponential isotropic hardening law $K(\alpha_i)$ according to [11,12]. To consider the nonlinear hardening behavior, Eq. (10) is reformulated to Eq. (13) considering the exponential hardening law [43] with Q_i and b_i being the hardening parameters in the decisive direction i.

$$\begin{aligned}
f(\boldsymbol{\sigma}, \alpha) &= \sqrt{\boldsymbol{\sigma}^{\mathrm{T}} : \tilde{\mathbf{A}} : \boldsymbol{\sigma}} - (f_{\mathrm{y},i} + K(\alpha_i)) \\
&= \sqrt{\boldsymbol{\sigma}^{\mathrm{T}} : \tilde{\mathbf{A}} : \boldsymbol{\sigma}} - (f_{\mathrm{y},i} + Q_i(1 - e^{-b_i\alpha_i}))
\end{aligned} \tag{13}$$

Consequently, b_i in Eq. (13) defines the shape of the exponential function and Q_i, is the difference between ultimate and yield strength, which defines the magnitude of the exponential function. The input material properties for the numerical analysis are listed in Table 1.

According to [44], the evolution of plastic strain $\dot{\varepsilon}^{\mathrm{p}}$ is defined by the associative flow rule as

$$\dot{\varepsilon}^{\mathrm{p}} = \Delta\lambda \frac{\partial f}{\partial \boldsymbol{\sigma}}, \tag{14}$$

with the plastic consistency parameter $\Delta\lambda$. The hardening variable α is defined by considering the hardening law as

$$\dot{\alpha} = \Delta\alpha \frac{\partial f}{\partial \alpha} = \Delta\lambda \frac{\partial f}{\partial q}\frac{\partial q}{\partial \alpha} = \Delta\lambda \frac{\partial q}{\partial \alpha}, \tag{15}$$

since $\partial f/\partial q = 1$ and $\Delta\lambda = \Delta\alpha$.

Finally, the Kuhn–Tucker loading/unloading conditions need to be fulfilled

$$\Delta\lambda \geq 0, \quad f(\boldsymbol{\sigma},\alpha) \leq 0, \quad \Delta\lambda f(\boldsymbol{\sigma},\alpha) = 0, \tag{16}$$

as well as the consistency conditions

$$\Delta\lambda \dot{f}(\boldsymbol{\sigma},\alpha) = 0, \quad \text{if} \quad f(\boldsymbol{\sigma},\alpha) = 0. \tag{17}$$

With all conditions being fulfilled, the elasto-plastic tangent modulus is expressed according to [42] as

$$\mathbf{C}_{\text{ep}} = \begin{cases} \mathbf{C}_0 - \dfrac{\mathbf{C}_0 : \dfrac{\partial f}{\partial \boldsymbol{\sigma}} \otimes \mathbf{C}_0 : \dfrac{\partial f}{\partial \boldsymbol{\sigma}}}{\mathbf{C}_0 : \dfrac{\partial f}{\partial \boldsymbol{\sigma}} : \dfrac{\partial f}{\partial \boldsymbol{\sigma}} + \dfrac{\partial f}{\partial q} : \dfrac{\partial q}{\partial \alpha}} & \text{if } \Delta\lambda > 0 \\ \mathbf{C}_0 & \text{if } \Delta\lambda = 0. \end{cases} \tag{18}$$

The algorithmic treatment of the stated plasticity is performed according to [30] and for the sake of completeness stated in Appendix B.

2.2. Brittle damage (tension and shear)

Beyond the linear elastic material range, softening of the material starts, which can be represented by CDM [14]. The onset of damage mechanisms, such as micro-cracking, are defined by damage initiation criteria in Section 2.2.1. The evolution of micro-cracks is characterized by the damage evolution laws using different scalar damage variables in Section 2.2.2, which can occur simultaneously. The propagation of the damage is dependent on the orthotropic material direction and the load-sign, and the propagation continues until macro-cracks evolve and failure occurs.

Taking effects of possible stress interactions into account, various damage initiation criteria are used in the literature inter alia in [9,10,17,19]. Among these, four different stress-based damage initiation criteria are selected and compared analytically in this section. The first criterion, Tsai–Wu [10], initiates damage by accounting for interaction of normal stresses in tensor formulation with only one closed surface. The second criterion, Hashin [19], originating from fiber composites, introduces four interactive failure criteria for four different failure modes with quadratic functions based on the stress invariants. More recently, Sandhaas [17] further adapted the latter criterion for wood by differentiating between eight different failure modes. And finally, a separated damage mode criterion with piece-wise continuously differentiable maximum stress functions for the single failure variables is discussed.

These four different analytical criteria represent existing and frequently considered damage initiation criteria for wood, besides phenomenologically based single-surface-plasticity-models which take strength and assumed interaction factors from experimental results into account as e.g. in [11,12]. They are validated in Sections 4.1 and 4.2 and further applied and compared on a tensile tested board with known fiber deviation in Section 4.3.

2.2.1. Damage initiation

(a) Tsai–Wu damage initiation criterion [10]
This criterion is represented by a single elliptical surface without distinction between failure modes. Thus compression and tension cannot be considered separately, which is the case in the other models in the following paragraphs. The tensor formulation is stated analytically in Eq. (19). This formulation is based on normal and shear stresses considering their interaction:

$$\begin{aligned} &\mathrm{F}_1\hat{\sigma}_{11} + \mathrm{F}_2\hat{\sigma}_{22} + \mathrm{F}_3\hat{\sigma}_{33} + \mathrm{F}_{11}\hat{\sigma}_{11}^2 + \mathrm{F}_{22}\hat{\sigma}_{22}^2 + \mathrm{F}_{33}\hat{\sigma}_{33}^2 + \\ &2\mathrm{F}_{12}\hat{\sigma}_{11}\hat{\sigma}_{22} + 2\mathrm{F}_{23}\hat{\sigma}_{22}\hat{\sigma}_{33} + 2\mathrm{F}_{13}\hat{\sigma}_{11}\hat{\sigma}_{33} + \\ &\mathrm{F}_{44}\hat{\sigma}_{13}^2 + \mathrm{F}_{55}\hat{\sigma}_{23}^2 + \mathrm{F}_{66}\hat{\sigma}_{12} \leq 1. \end{aligned} \tag{19}$$

with

$$\begin{aligned} &\mathrm{F}_1 = \frac{1}{f_{\text{t,L}}} - \frac{1}{f_{\text{c,L}}}, \quad \mathrm{F}_2 = \frac{1}{f_{\text{t,R}}} - \frac{1}{f_{\text{c,R}}}, \quad \mathrm{F}_3 = \frac{1}{f_{\text{t,T}}} - \frac{1}{f_{\text{c,T}}}, \\ &\mathrm{F}_{11} = \frac{1}{f_{\text{t,L}} f_{\text{c,L}}}, \quad \mathrm{F}_{22} = \frac{1}{f_{\text{t,R}} f_{\text{c,R}}}, \quad \mathrm{F}_{33} = \frac{1}{f_{\text{t,T}} f_{\text{c,T}}}, \\ &\mathrm{F}_{44} = \frac{1}{f_{\text{v,LT}}^2}, \quad \mathrm{F}_{55} = \frac{1}{f_{\text{v,RT}}^2}, \quad \mathrm{F}_{66} = \frac{1}{f_{\text{v,LR}}^2}, \\ &\mathrm{F}_{12} = -\frac{1}{2}\frac{1}{\sqrt{f_{\text{t,L}} f_{\text{c,L}} f_{\text{t,R}} f_{\text{c,R}}}}, \quad \mathrm{F}_{13} = -\frac{1}{2}\frac{1}{\sqrt{f_{\text{t,L}} f_{\text{c,L}} f_{\text{t,T}} f_{\text{c,T}}}}, \\ &\mathrm{F}_{23} = -\frac{1}{2}\frac{1}{\sqrt{f_{\text{t,R}} f_{\text{c,R}} f_{\text{t,T}} f_{\text{c,T}}}}. \end{aligned} \tag{20}$$

This failure criterion has limited physical meaning for wood because e.g. the material resistance F_1 in Eq. (20) depends on a combination of tensile and compression strength.

(b) Hashin damage initiation criterion [19]
This criterion was primarily developed for fiber composites with transversely isotropic material properties, where it is necessary to distinguish between fiber- and matrix-failure. It is based on the stress invariants and is separated into different criteria according to the fiber- and matrix-behavior. Four stress-interactive failure criteria represent four different failure modes: parallel failure in tension $F_{t,\parallel}$ or compression $F_{c,\parallel}$ and matrix failure in compression $F_{c,\perp}$ or tension $F_{t,\perp}$. In different failure modes, stress interactions are considered differently as shown in Eq. (21) and (22). Hashin further concluded that only linear and quadratic terms are necessary for the simplest fitting solution.

$$\begin{aligned} &\hat{\sigma}_{11} \geq 0: \quad \mathrm{F}_{\text{t,}\parallel} = \left(\frac{\hat{\sigma}_{11}}{f_{\text{t,}\parallel}}\right)^2 + \frac{\hat{\sigma}_{12}^2 + \hat{\sigma}_{13}^2}{f_{\text{v,12}}^2} \leq 1 \\ &\hat{\sigma}_{11} < 0: \quad \mathrm{F}_{\text{c,}\parallel} = \left(\frac{\hat{\sigma}_{11}}{f_{\text{c,}\parallel}}\right)^2 \leq 1 \end{aligned} \tag{21}$$

$$\begin{aligned} \hat{\sigma}_{22} + \hat{\sigma}_{33} > 0: \quad \mathrm{F}_{\text{t,}\perp} &= \frac{(\hat{\sigma}_{22} + \hat{\sigma}_{33})^2}{f_{\text{t,}\perp}^2} + \frac{(\hat{\sigma}_{23}^2 - \hat{\sigma}_{22}\hat{\sigma}_{33})}{f_{\text{v,23}}^2} \\ &+ \frac{\hat{\sigma}_{12}^2 + \hat{\sigma}_{13}^2}{f_{\text{v,12}}^2} \leq 1 \\ \hat{\sigma}_{22} + \hat{\sigma}_{33} < 0: \quad \mathrm{F}_{\text{c,}\perp} &= \left[\left(\frac{f_{\text{c,}\perp}}{2f_{\text{v,23}}}\right)^2 - 1\right]\left(\frac{\hat{\sigma}_{22} + \hat{\sigma}_{33}}{f_{\text{c,}\perp}}\right) \\ &+ \frac{(\hat{\sigma}_{22} + \hat{\sigma}_{33})^2}{4f_{\text{v,23}}^2} + \frac{(\hat{\sigma}_{22} + \hat{\sigma}_{33})^2}{f_{\text{c,}\perp}^2} \\ &+ \frac{(\hat{\sigma}_{23}^2 - \hat{\sigma}_{22}\hat{\sigma}_{33})}{f_{\text{v,23}}^2} + \frac{\hat{\sigma}_{12}^2 + \hat{\sigma}_{13}^2}{f_{\text{v,12}}^2} \leq 1 \end{aligned} \tag{22}$$

(c) Sandhaas damage initiation criterion [17]
This mixed phenomenological and analytical criterion differentiates between eight failure modes. Longitudinal normal stresses are treated separately in compression and in tension, and normal and shear stresses are combined in quadratic criteria for transverse tension and shear failure modes, as presented in Eq. (23)- (25).

$$\begin{aligned} &\hat{\sigma}_{11} \geq 0: \quad \mathrm{F}_{\text{t,L}} = \frac{\hat{\sigma}_{11}}{f_{\text{t,L}}} \leq 1 \\ &\hat{\sigma}_{11} < 0: \quad \mathrm{F}_{\text{c,L}} = \frac{-\hat{\sigma}_{11}}{f_{\text{c,L}}} \leq 1 \end{aligned} \tag{23}$$

$$\begin{aligned} &\hat{\sigma}_{22} \geq 0: \quad \mathrm{F}_{\text{t,R}} = \frac{\hat{\sigma}_{22}^2}{f_{\text{t,R}}^2} + \frac{\hat{\sigma}_{12}^2}{f_{\text{v,LR}}^2} + \frac{\hat{\sigma}_{23}^2}{f_{\text{v,RT}}^2} \leq 1 \\ &\hat{\sigma}_{22} < 0: \quad \mathrm{F}_{\text{c,R}} = \frac{-\hat{\sigma}_{22}}{f_{\text{c,R}}} \leq 1 \\ &\qquad\quad \mathrm{F}_{\text{v,R}} = \frac{\hat{\sigma}_{12}^2}{f_{\text{v,LR}}^2} + \frac{\hat{\sigma}_{23}^2}{f_{\text{v,RT}}^2} \leq 1 \end{aligned} \tag{24}$$

$$\begin{aligned}
\hat{\sigma}_{33} < 0: \quad & \mathrm{F_{c,T}} = \frac{-\hat{\sigma}_{33}}{f_{\mathrm{c,T}}} \leq 1 \\
\hat{\sigma}_{33} \geq 0: \quad & \mathrm{F_{t,T}} = \frac{\hat{\sigma}_{33}^2}{f_{\mathrm{t,T}}^2} + \frac{\hat{\sigma}_{13}^2}{f_{\mathrm{v,LT}}^2} + \frac{\hat{\sigma}_{23}^2}{f_{\mathrm{v,RT}}^2} \leq 1 \\
& \mathrm{F_{v,T}} = \frac{\hat{\sigma}_{13}^2}{f_{\mathrm{v,LT}}^2} + \frac{\hat{\sigma}_{23}^2}{f_{\mathrm{v,RT}}^2} \leq 1
\end{aligned} \tag{25}$$

(d) Separated damage mode (SDM) initiation criterion
This is the only criterion which does not assume interactions of stresses, but treats every stress direction separately. Thus, nine different failure modes are separated in maximum stress functions.

$$\begin{aligned}
& \mathrm{F_{c/t,L}} = \frac{|\hat{\sigma}_{11}|}{f_{\mathrm{c/t,L}}} \quad \mathrm{F_{c/t,R}} = \frac{|\hat{\sigma}_{22}|}{f_{\mathrm{c/t,R}}} \quad \mathrm{F_{c/t,T}} = \frac{|\hat{\sigma}_{33}|}{f_{\mathrm{c/t,T}}} \\
& \mathrm{F_{v,LR}} = \frac{\hat{\sigma}_{12}}{f_{\mathrm{v,LR}}} \quad \mathrm{F_{v,LT}} = \frac{\hat{\sigma}_{13}}{f_{\mathrm{v,LT}}} \quad \mathrm{F_{v,RT}} = \frac{\hat{\sigma}_{23}}{f_{\mathrm{v,RT}}}
\end{aligned} \tag{26}$$

Due to the scatter of material properties and the strong dependence on the orthotropic material directions, it is difficult to verify which damage initiation criterion is the best representation. Commonly, it can be pointed out that all damage initiation criteria shall agree in uniaxial principal stress directions. The assumption that stress interaction leads to strength reduction is not fully confirmed yet, although some biaxial loading experiments [33] tried to quantify the influence of biaxial loading on strength and failure modes. However it is still unknown how the stress interactions evolve in orthotropic heterogeneous space, since the mentioned models are simplifying the cellular structure of the material to a continuum transverse isotropic material.

A slightly different approach to single failure surfaces, as e.g. Tsai–Wu, is applied in Hashin, Sandhaas and SDM: The interaction of different stresses is considered by means of using not only one damage scalar but multiple damage variables for the orthotropic directions instead. As one or several damage variables start to evolve, stiffness gets weakened, and consequently stress redistribution will occur. This separate consideration can also be seen as an analogous procedure for stress interactions and makes the differentiation between mixed failure modes possible.

After the initiation of damage indicated by $F_i \geq 1$, the tensor of damage variables $\mathbf{d}(\kappa_i)$ is being identified for modifying the compliance matrix in Eq. (33) separately in each direction. κ_i is defined as the state variable and specified as $\kappa_i = \max\{1, \max(\mathrm{F}_i^{\mathrm{incr}})\}$ for i representing the different failure modes according to the damage initiation criterion. The limit state function ϕ_i in this case is then expressed as a function of F_i and the state variable κ_i as:

$$\phi_i(\mathrm{F}_i, \kappa_i) = \mathrm{F}_i - \kappa_i \leq 0. \tag{27}$$

Similar to plasticity, the damage threshold values are expressed by the Kuhn–Tucker conditions:

$$\phi_i \leq 0, \quad \dot{\kappa}_i \geq 0, \quad \dot{\kappa}_i \phi_i = 0, \tag{28}$$

and the consistency condition

$$\kappa_i \dot{\phi}_i = 0 \quad \text{if} \quad \phi_i = 0. \tag{29}$$

2.2.2. Damage evolution

After damage initiation, different damage variables of the damage tensor can propagate dependent on the damage propagation law in compression and in tension. Multiple stresses and their interaction effects are considered by combining the simultaneously evolving damage variables in one damaged stiffness matrix.

Material properties such as the fracture energy and elastic moduli in each specific material direction are considered in the given damage propagation laws following linear softening according to [17], as

$$d_{\mathrm{t/v},i}(\kappa_i) = 1 - \frac{1}{f_{\mathrm{t},i}^2 - 2g_{\mathrm{f},i}\mathrm{E}_i}\left(f_{\mathrm{t},i}^2 - \frac{2g_{\mathrm{f},i}\mathrm{E}_i}{\kappa_i}\right), \tag{30}$$

with the maximum strength $f_{\mathrm{t/v},i}$, modulus of elasticity E_i, fracture energy $g_{\mathrm{f},i}$, which includes the characteristic element length as given in Eq. (47), in the same material direction i.

Considering a different damage propagation in the ductile failure modes for wood under compression, shown in Fig. 1, perfect plasticity according to [17] is modeled as,

$$d_{\mathrm{c},i}(\kappa_i) = 1 - \frac{1}{\kappa_i}. \tag{31}$$

All scalar damage variables may appear simultaneously and take values between 0 for undamaged and 1 for completely damaged. Only the differentiation between compression and tension in normal directions $i = L, R, T$ is performed using the Macaulay operator according to

$$d_i = d_{\mathrm{c},i}\frac{\langle\hat{\sigma}_{\mathrm{ii}}\rangle}{|\hat{\sigma}_{\mathrm{ii}}|} + d_{\mathrm{t},i}\frac{\langle\hat{\sigma}_{\mathrm{ii}}\rangle}{|\hat{\sigma}_{\mathrm{ii}}|}. \tag{32}$$

These damage propagation laws can be adapted to other degradation laws e.g. exponential functions for softening in tension and compression or densification laws in compression.

Once the scalar damage variables are computed, the compliance matrix is modified as

$$\mathbf{D}_{\mathrm{d}} = \begin{bmatrix}
\frac{1}{(1-\mathrm{d_L})\mathrm{E}_{11}} & \frac{-\nu_{21}}{\mathrm{E}_{22}} & \frac{-\nu_{31}}{\mathrm{E}_{33}} & 0 & 0 & 0 \\
\frac{-\nu_{12}}{\mathrm{E}_{11}} & \frac{1}{(1-\mathrm{d_R})\mathrm{E}_{22}} & \frac{-\nu_{32}}{\mathrm{E}_{33}} & 0 & 0 & 0 \\
\frac{-\nu_{13}}{\mathrm{E}_{11}} & \frac{-\nu_{23}}{\mathrm{E}_{22}} & \frac{1}{(1-\mathrm{d_T})\mathrm{E}_{33}} & 0 & 0 & 0 \\
0 & 0 & 0 & \frac{1}{(1-\mathrm{d_{v,LR}})\mathrm{G}_{12}} & 0 & 0 \\
0 & 0 & 0 & 0 & \frac{1}{(1-\mathrm{d_{v,LT}})\mathrm{G}_{13}} & 0 \\
0 & 0 & 0 & 0 & 0 & \frac{1}{(1-\mathrm{d_{v,RT}})\mathrm{G}_{23}}
\end{bmatrix}, \tag{33}$$

which can be inserted in Eq. (3).

3. Implementation and workflow

The elasto-plastic damaging material law is implemented in the software ABAQUS/Standard (Simulia 6.14, from Dassault Systems) as a user defined material subroutine UMAT. The local principal material directions are determined by the fiber angle and ring angle via the transformation matrix locally at each integration point as presented in [7].

The numerical workflow is controlled by strain-based increments, which are divided into N defined time intervals $[t_n, t_{n+1}]$ over a fictive time T.

The total strain is composed of the elastic and plastic strain, where the plastic part is implemented via the closest-point-projection algorithm of Simo and Hughes [42]. The scheme is described in detail in Appendix B following the main steps of [30]. Furthermore, after the tangent plastic stiffness matrix has been calculated, damage initiation criteria are being checked and consequently damage variables are being calculated, which reduces the entries of the tangent plastic stiffness matrix, following the principle of CDM. The crack band method according to [45] is implemented to alleviate mesh dependency. Once one damage variable reaches the value of 1 in all integration points of an element, the element is deleted. This is supposed to represent cracks in a simplified way and avoids highly distorted elements.

4. Numerical examples with experimental validation

Although the developed model is applicable to different wood species, European beech (*Fagus Sylvatica* L.) is chosen for validation, due to the importance and motivation stated in Section 1. The focus of this investigation is on the validation of the numerical material model for the 3D post-elastic material behavior. Model complexity is increased

Table 1
Summary of material properties for European Beech (*Fagus Sylvatica* F.).

			Literature							Simulation values
			[40]	[46]	[17]	[47]	[3]	[48] (GAU)	[48] (THR)	
Elastic	E_L	[MPa]	14 000	10 560	13 000	13 700		13 509	12 741	12 500
	E_R		2280	1510	860	2240		1722	2036	2050
	E_T		1160	730	860	1140		707	913	810
	G_{LR}		1640	1240	810	1610				1640
	G_{LT}		1080	930	810	1060				1080
	G_{RT}		470	380	59	460				470
	ν_{LR}	[–]	0.43	0.43		0.450		0.32	0.40	0.43
	ν_{LT}		0.58	0.58		0.510		0.30	0.40	0.58
	ν_{RT}		0.61	0.61		0.750		0.61	0.66	0.61
	ν_{RL}		0.04	0.04		0.073				0.04
	ν_{TL}		0.04	0.04		0.044				0.04
	ν_{TR}		0.31	0.31		0.360		0.26	0.29	0.31
Post-elastic	$f_{t,L}$	[MPa]	96.7	96.7	41.0		135.0	139.4	121.7	134.0
	$f_{t,R}$		14.7	19.5	1.0		7.0	18.2	17.9	18.0
	$f_{t,T}$		8.9	8.9	1.0		7.0	8.0	6.2	7.0
	$f_{c,L}$		45.0		45.0		57.0	57.0	61.9	62.0
	$f_{c,R}$		11.0		14.2		10.0	11.9	15.5	15.5
	$f_{c,T}$		6.0		14.2		10.0	5.7	6.7	7.0
	$f_{v,LR}$		13.8		6.9		12.7–14.8			14.0
	$f_{v,LT}$		17.7		6.9		15.7–19.7			18.0
	$f_{v,RT}$		15.0		0.5					15.0
	$G_{f,L}$	[N/mm]			10.00					10.00
	$G_{f,R/T}$		0.32–0.73		0.71		0.32–0.73			0.71
	$G_{f,v}$				1.20					1.20
	$G_{f,roll}$		0.55–0.69		0.60		0.55–0.69			0.60
Numerical	Q_L	[MPa]								9.3
	Q_R									5.4
	Q_T									2.5
	b_L	[–]								300
	b_R									500
	b_T									250

Table 2
General characteristics of experimental test data [48] and its scatter for compression (c) and tension (t) in the three directions (L,R,T) for the amount of test samples (n); standard deviation is given in the brackets after the mean value.

i	n	f_i [MPa]	E_i [MPa]	[48]
c,L	47	61.9 (4.3)	12820 (1337)	
c,R	49	15.5 (0.9)	2082 (127)	(THR)
c,T	49	6.7 (0.4)	818 (32)	
t,L	43	139.4 (38.5)	13509 (1652)	
t,R	29	18.2 (1.0)	1722 (74)	(GAU)
t,T	30	8.0 (0.5)	707 (28)	

gradually, thus two clear wood benchmark examples and one example with slight fiber deviation are analyzed for axial loading conditions. These examples are modeled with the material model presented in Sections 2 and 3 and compared to experimental results. To be able to distinguish and study different failure modes, the first example focuses on the nonlinear ductile material behavior under compression, while the second example on brittle softening under tension/shear. The third example demonstrates the application of the numerical model on sawn timber with local fiber deviations for strength prediction.

Literature values for the input material parameters such as elastic moduli, shear moduli, Poisson ratios, as well as strength values in compression and tension, and fracture energies are listed in Table 1. Differences can be observed for the different references listed which might be a consequence of different mechanical testing setups, strain/stress measurement techniques, size effects, etc. However, the numerical model needs to contain an appropriate set of input parameters that represent the material well, considering the scatter in the material properties. Consequently, plausible values in the range of literature and experimental values are taken as input parameters for this model and listed in the last column of Table 1.

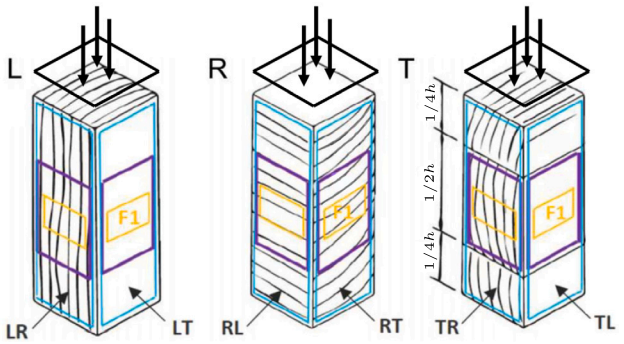

Fig. 3. Exemplary representation of the compression test cubes under compression loading with regard to the alignment in longitudinal, radial or tangential direction [48].

4.1. Compression cuboid with square cross-section

For the validation of the plastic material behavior experimental test results from [48] have been used in this study. Similar to [48], samples with rectangular shapes, and dimensions of $45 \times 15 \times 15$ mm^3 ($l \times w \times t$) in accordance with DIN 52192 have been numerically simulated, see Fig. 3. A total number of 20 tests in each direction have been analyzed separately in this study. Table 2 summarizes the main characteristics of the experimental data focusing on the mean and standard deviation of the measured stiffness/strength and shows the heterogeneous material character. The given material parameters are in accordance with Table 1, except the elastic moduli in compression, which were simplified to be the same as the elastic moduli in tension.

4.1.1. Mechanical test setup

All samples were climatized to 20°C/65% relative humidity (RH) and tested in 20°C/50% RH climatized conditions. The mechanical

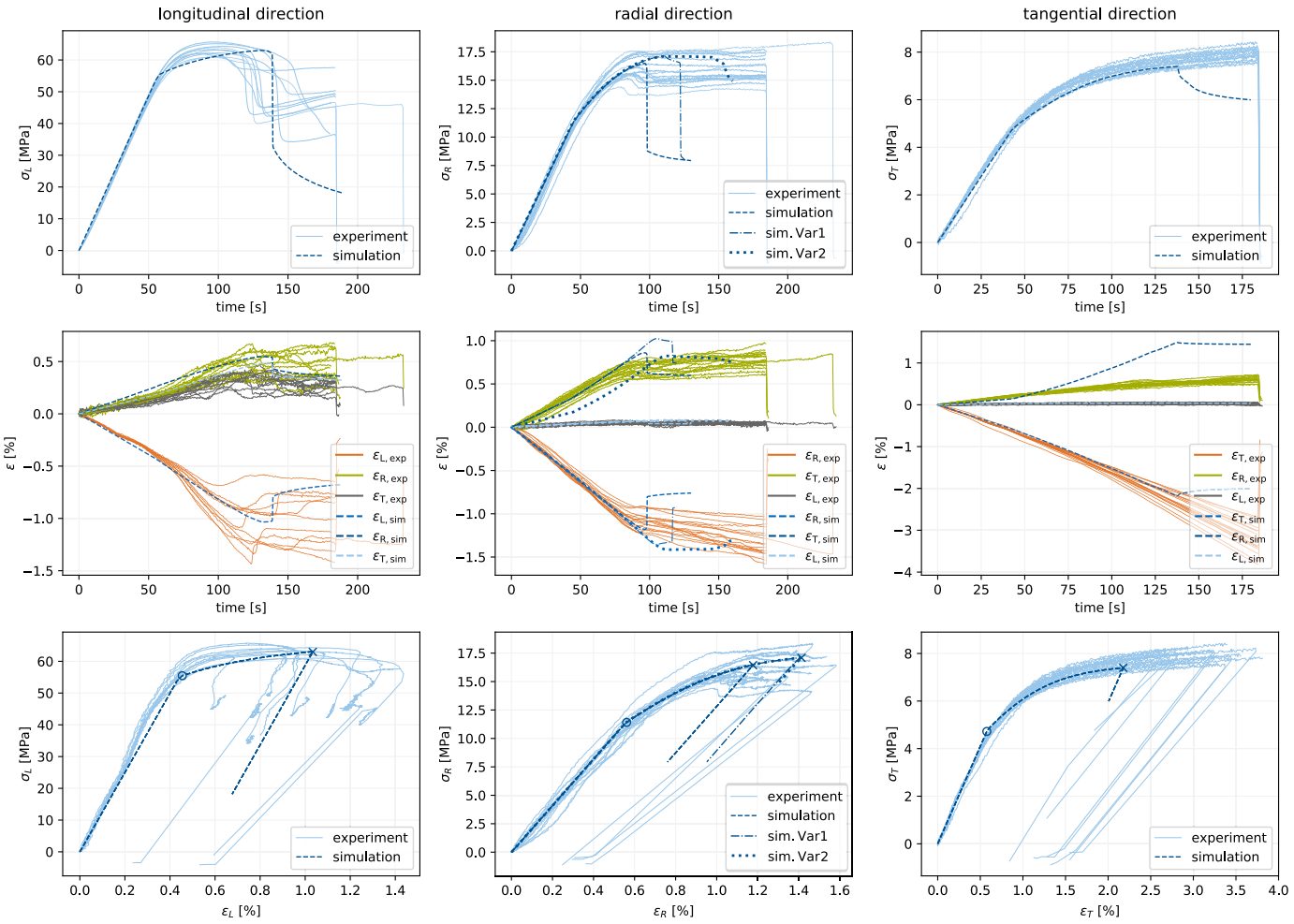

Fig. 4. Stress in loading direction and strain in the three orthogonal directions from experimental and numerical tests in longitudinal (first column), radial (second column) and tangential (third column) loading direction with marked yield initiation (o) and damage initiation (x). Sim.Var1 and sim.Var2 refer to the simulation with modified material properties as discussed in Section 4.1.3.

testing setup and procedure was executed with a universal testing machine Zwick/Roell Z100 and linked to a 100 kN load cell. The displacement rate of the compression load was set to 0.6 mm/min for reaching an initial strain rate of 1%/min. The experiments were terminated when a clear drop in the force occurred. For the detection of the surface strain with the digital image correlation (DIC) system (Aramis, GOM GmbH, Braunschweig, Germany), it was necessary to cover the surfaces with a white primer and random black sparkles distributed on the samples surfaces. The optical measurement system was positioned perpendicular to the edge of the test specimen such that the strain was measured on two sides in F1 (10 × 13 mm) as visualized in Fig. 3. Three different strain directions were measured: $\varepsilon_{\parallel}$ in loading direction and $\varepsilon_{\perp}$ in both directions perpendicular to loading direction. Thus it was possible to evaluate three Poisson ratios in the elastic range and the plastic strain in all directions in the post-elastic range.

4.1.2. Numerical test setup

The cuboids are modeled in three different configurations of fiber orientation, following the experimental tests. The orientation is induced by a global Cartesian coordinate system. After performing the mesh convergence studies, the appropriate mesh size is chosen for the calculations. In this study, linear solid brick elements C3D8 are used for the simulations. The bottom surface is clamped with all degrees of freedom fixed, which assumes high friction between the supporting plate and the test specimens as observed in the experimental tests. The top surface is coupled to a reference point, where the compression stress was induced by a prescribed displacement similar to the experimental tests with a maximum increment size of 0.01 mm. Degrees of freedom in the other directions are fixed similarly to the bottom surface, assuming infinitesimal friction between the supporting plate and the test specimen.

The elastic material properties for the model are given in Table 1. The elasto-plastic damaging material model presented in Section 2 is applied to the three cuboids. For the post-elastic behavior, yield compression strength in longitudinal direction was set to $f_{y,\mathrm{L}} = 0.85 \cdot f_{\mathrm{c,L}}$ and in radial as well as in tangential direction to $f_{y,\mathrm{R/T}} = 0.65 \cdot f_{\mathrm{c,R/T}}$, similar to [11]. Accordingly, the hardening moduli, Q_i are defined since the difference between the compression strength and the yield strength in the same directions with $Q_{\mathrm{L}} = 0.15 \cdot f_{\mathrm{c,L}}$, $Q_{\mathrm{R/T}} = 0.35 \cdot f_{\mathrm{c,R/T}}$ is dependent on the decisive loading directions as outlined in Section 2.1. Similarly to the experiments, the strain is evaluated in the area 'F1' of the specimen visualized in Fig. 3 for the simulations.

4.1.3. Results and validation

The main focus of this investigation is to analyze the stress in loading direction as well as the strain in all three orthotropic material directions, since all directions contribute to the material strength in a 3D board with fiber deviation. The elastic and post-elastic results from the experimental and numerical compression tests are visualized in Fig. 4. The first row of diagrams in Fig. 4 shows the stress over time, whereas the second row represents the strain response in all directions over time and the third row of diagrams illustrates the stress–strain

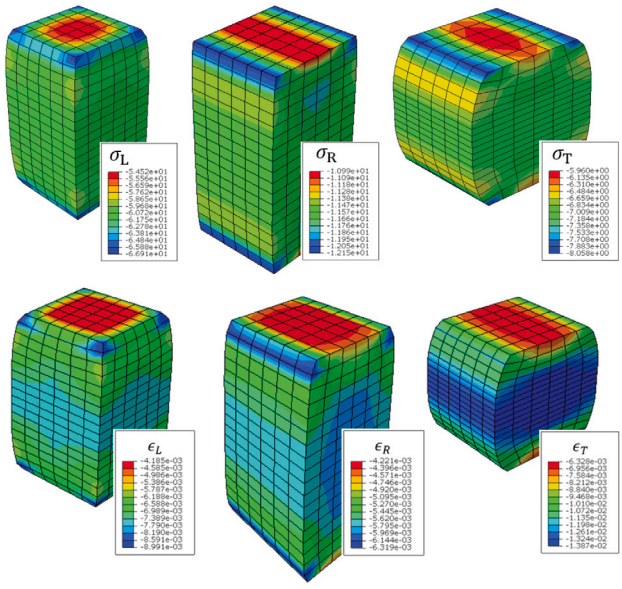

Fig. 5. Numerical strain and stress in loading direction of compression tests during nonlinear hardening scaled by factor 50.

graph in the respective loading direction: in longitudinal fiber direction (first column), in radial direction (second column) and in tangential direction (third column).

The experimental strains are averaged over the area 'F1', shown in Fig. 3 and the engineering stress is calculated by dividing the applied force by the initially measured cross-sectional area. The same is done for the numerical stress–strain results indicated in Fig. 4. Further, numerical stress and strain results are visualized in Fig. 5 in the post-elastic hardening phase.

Looking at the results in the third row of Fig. 4, all three global stress–strain curves show an overall representative material behavior. Experimental results in longitudinal direction demonstrate a larger scatter in comparison to the experimental results in radial and tangential direction, which is also captured by the mean and standard deviation values for stiffness and strength in Table 2.

Generally, in all three material directions, the elastic material behavior is corresponding well for both numerical and experimental results. Also after the elastic range, when the yield stress is reached and hardening is initiated, good conformity in the response between experimental and simulation is achieved. When the load is considered in radial or tangential direction (second and third column), the yield stress already occurs at around 65% of the maximum stress and the nonlinear plastic behavior is more pronounced.

Looking at the strain behavior of the experimentally tested specimens in the second row of Fig. 4, differences are visible in evolution of strains in the three orthotropic material directions and for all loading configurations due to its input parameters. This material behavior is mostly also covered in the numerical results. The increase in slope of the numerical strain in the plastic region is dependent on the adapted Hill-plasticity criterion and the exponential hardening law, controlled according to the exponential factor b_i in Eq. (13).

The influence of the boundary conditions and its resulting stress concentrations, the influence of the Poisson ratios, and the influence of the damage law are analyzed and shown exemplarily for loading in radial direction (second column in Fig. 4). By applying a friction coefficient of 0.3 between the loading plate and wood, stress concentrations are amplified in the regions of boundary conditions. The plastic strain in the middle of the sample is not directly influenced, however its effect is visible in the initiation and evolution of damage

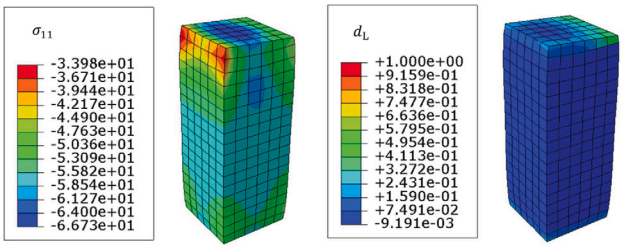

Fig. 6. Stress σ_{11} in [MPa] and according damage variable d_L for loading in fiber direction at the time step of 130 s capturing fiber buckling in the boundary regions.

in compression (crushing cells). Not only damage in loading direction d_R, but also damage in tangential direction d_T is initiated. Once damage in loading direction (radial) starts, the stress redistributes also in tangential direction. This effect elevates even more due to the influence of the boundary conditions with high friction, since ultimate compressive strength is reached earlier. Subsequently, it results in the drop of stress and strain visualized in the dashed curves in Fig. 4, second column at 100 seconds. In a separate set of simulations (Var1) the boundary conditions of the model are changed. Different friction coefficients between loading plate and test sample are analyzed and a friction coefficient of 0.1 is visualized in Fig. 4-Var1. Once friction is reduced, damage in tangential direction d_T is postponed and, the second drop in stress/strain occurs at 125 seconds, as visualized in the dashed–dotted curve in the same graph (Fig. 4-Var1). Furthermore, stress redistributions are mostly influenced by the orthotropic material law and the high Poisson's ratios for wood. While in literature, as presented in Table 1, scatter in material properties are given, the effect of less stress redistributions to the tangential direction according to $\nu_{RT} = 0.31$ is visualized in the dotted line (Fig. 4-Var2): Damage in the second direction initiates later causing the second drop in stress/strain at around 150 s.

Wood as a naturally grown material has a considerable amount of scatter in its material properties and its mechanical behavior. "Perfect" small clear wood samples do not exist. Thus this validation example does not aim to best fit the deterministic model to experimental data, but it rather aims to predict the mechanical behavior of this material. Therefore, sensitivity analysis of different numerical material models including different laws/parameters are performed in this study. It is also shown here, that preventing homogenization of the material gives a considerable variation of the results. Effects of several parameters are difficult to distinguish once more heterogeneities such as imperfections or fiber deviations are included in the model. Loading in fiber direction shows a stronger scatter of experimental values (stiffness, strength) in loading direction and than in radial and tangential directions as can be seen in Table 2 and in Fig. 4. The slope of strain-over-time (second row) increases until an abrupt drop in strain in fiber direction (and less pronounced also in radial and tangential direction) becomes noticeable. This indicates the buckling of the fibers in the local region near the boundary conditions and is also captured by the numerical model with an exaggerated strain drop. Subsequently, neither stress nor strain increase remarkably, which indicates the damaged crushed fibers. The material behavior at this point is further captured in Fig. 6 showing the compression cube with high stresses and local damage values around the fully constraint boundary conditions.

For loading in radial direction, the experimental results in the second column in Fig. 4 can be interpreted as follows. The experimental curves show slightly less scatter in the post-elastic nonlinear region. The strain in fiber direction remains around zero and the slope of strain-over-time in (radial) loading direction does not change significantly compared to the elastic range. After reaching the ultimate load the strain increases slightly and shows approximately perfect plasticity in

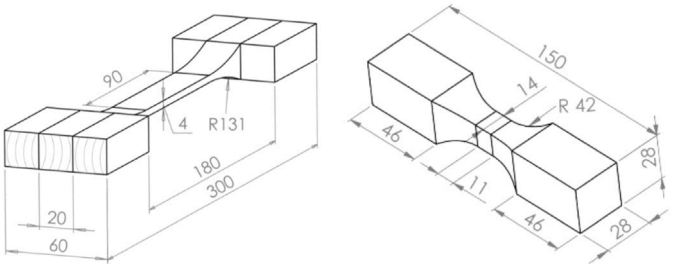

Fig. 7. Geometry of tensile dogbone test sample for loading in fiber direction (scaled, left) and for loading in radial/tangential direction (right) [48] with units in [mm].

radial direction. Comparing the simulation results with the experiments, one can see that the elastic and plastic strain in all directions seem congruent. The numerical strain in fiber directions remains zero. The sudden drop in stress and strain in the other directions is due to damage initiation in the areas of the clamped boundary conditions, where buckling of the fibers occurs and subsequently smaller increase in slope of strain results. It is exaggerated due to fully constrained boundary conditions in the simulation allowing no friction in second and third direction. Nevertheless, this damage can also be seen in both experimental and numerical results with the kink in the strain curves, marked by (x) in the numerical stress–strain-curve.

Loading in tangential direction indicates similar behavior like loading in radial direction: The strain in fiber direction remains zero. Meanwhile, the strain in tangential loading direction increases significantly after the elastic material range and the strain in radial direction remains nearly constant in the post-elastic material range. No softening is identifiable, but a pronounced nonlinear hardening behavior needs to be pointed out. This is also represented in the numerical model until a strain drop occurs due to damage at the boundary conditions similar to the behavior in radial or longitudinal direction visualized in Fig. 6.

Finally to summarize the results, simulation results and experimental results agree well. Therefore the elasto-plastic damage material model is able to capture the real behavior in all three directions for axial loading situations and material input parameters referring to literature values. Early fiber buckling due to fixed BCs can be pointed out as limitation of these validation results.

4.2. Tensile dogbone test

For the validation of the elasto-damaging constitutive law (Section 2.2) for brittle failure behavior, specimens with dogbone shape and different dimensions, as presented in Fig. 7 following DIN 52188, have been tested in tension in [48]. A total number of 20 tests have been evaluated separately in each direction in this study. Table 2 summarizes the main characteristics of the experimental data focusing on the mean and standard deviation of the measured stiffness and strength.

4.2.1. Mechanical test setup

All samples were climatized to 20°C/65% RH and tested in 20°C/50% RH climatized conditions. The mechanical test setup and procedure was executed with a universal testing machine Zwick/Roell Z100 and linked to a calibrated 5 kN load cell. The specimen was clamped with a clamping length of 60 mm by means of collets without wedge clamping effect, so that no pressure was generated in the testing direction during clamping. The geometrical dimension and the centered position of the samples reduced the stress situation to one decisive failure stress. In addition, the material for this test was selected in a way that the global clear wood material directions did not show visible fiber deviations.

The displacement rate of the tensile load was set to achieve a strain-rate of $0.95 - 1.05\%/\text{min}$. For the detection of the strain with DIC (Aramis, GOM GmbH, Braunschweig, Germany), the surfaces in the area of interest were covered with a random pattern. The measurement system was positioned in front of the test specimen and the strain was measured on the surface with a length of 50 mm in fiber loading direction and a length of 10 mm in radial/tangential loading directions. The width of the surface measurement was kept over the whole width of the test sample.

4.2.2. Numerical test setup

The dogbone-shaped specimens are modeled according to the experimental tests, where the orientation is induced by means of a global Cartesian coordinate system. Similar to the compression tests, after performing the mesh convergence test for this set of analysis an optimal mesh size, with respect to the model accuracy, resolution and computational costs has been selected for the simulations. C3D8 linear solid brick elements are used for the simulations. The bottom surface is fixed in loading direction and two edges of the surface are fixed in second or third direction. The top surface is constraint to a reference point with prescribed displacements in loading direction and fixed rotation around the loading axis. The displacement is induced with an increment size of 0.01 mm until the strength is reached. The elastic material properties as well as the strength and fracture energies for the model are given in Table 1. The elasto-plastic damaging material model, presented in Section 2.2, is applied and validated for this axial load case.

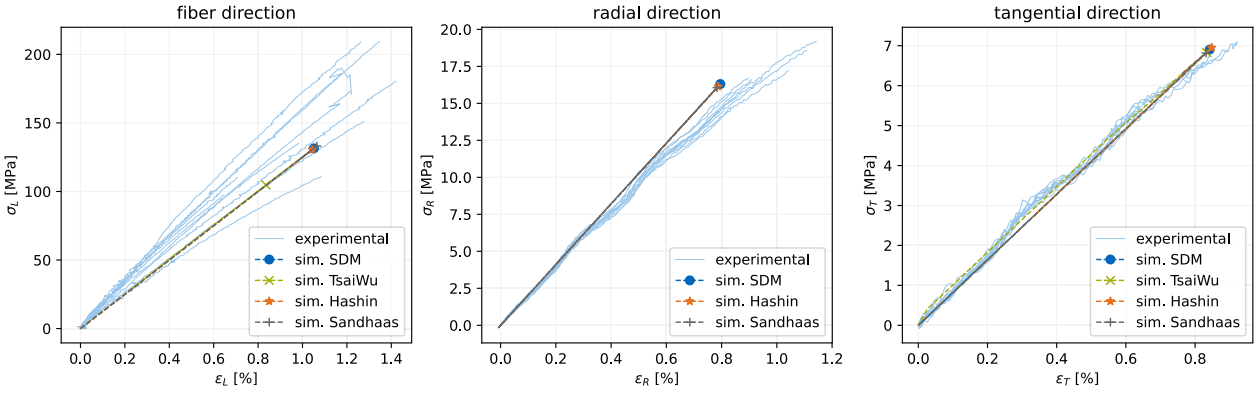

Fig. 8. Experimental and numerical global results of the dogbone-shaped tensile tests in all three directions.

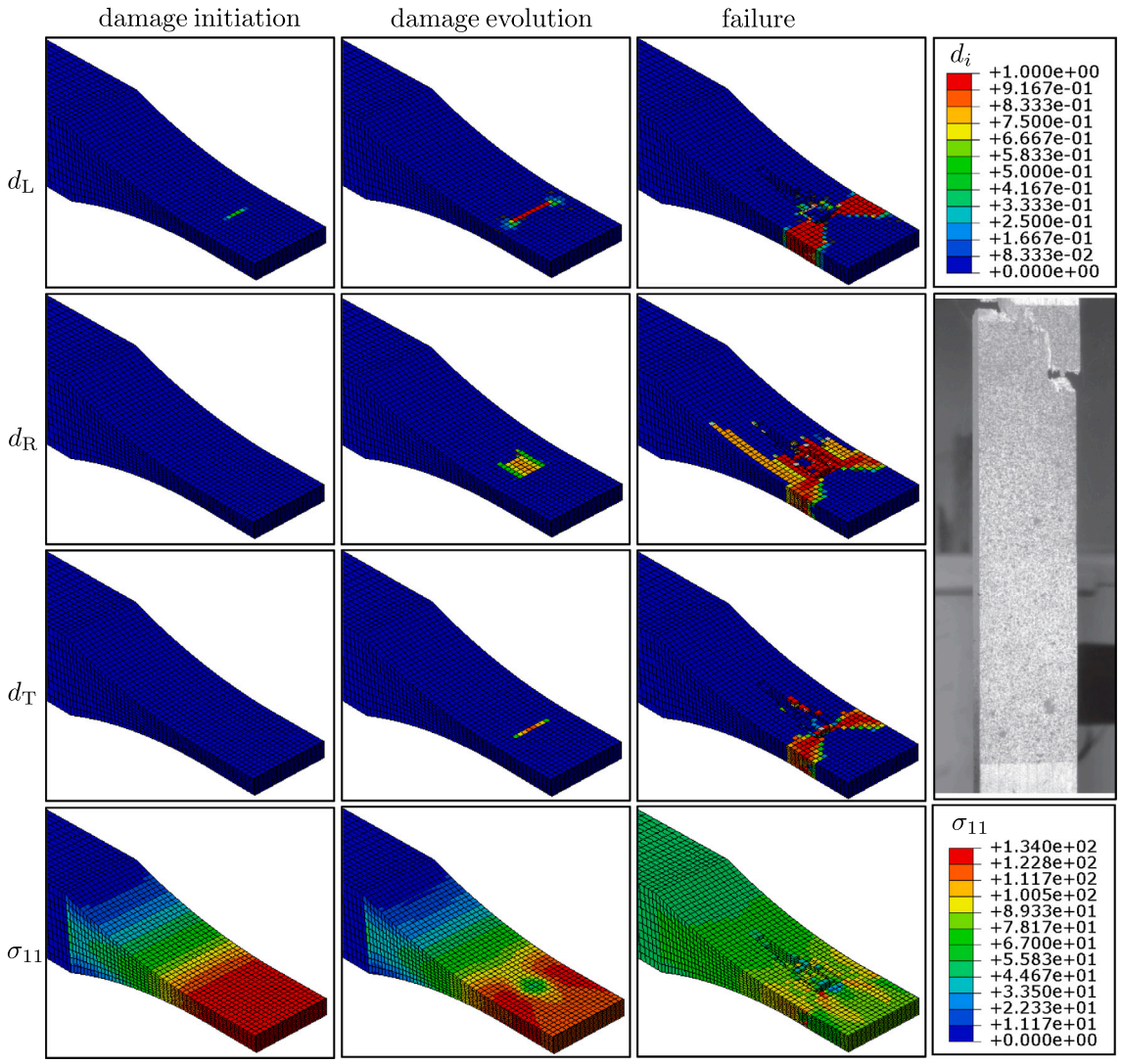

Fig. 9. Numerical evolution of the damage variables and the driving stress σ_{11} in [MPa] (rows) for the SDM criterion at different time steps (columns): Damage initiation, damage evolution and failure as well as the experimental failure mode for a representative experimental test sample (middle right).

4.2.3. Experimental validation and numerical results

For validation of the numerical results, global structural response (Fig. 8) and local damage evolution (Figs. 9, 10) are investigated. The global structural response is compared in the linear elastic range as well as for the stress peak at brittle failure. Different material behavior for the two different sample sizes (for loading in fiber direction and loading in radial/tangential direction) are shown in this figure. For loading in fiber direction, the stress–strain curves, failure modes of the experimental data, as well as the mean and standard deviation of the strength in Table 2 point out the high scatter of the material properties dependent on small deviations in the material orientation of the assumed clear wood samples. For loading in radial/tangential direction, the scatter of experimental data in Table 2 is smaller. Also the experimental stress–strain curves in Fig. 8 are aligned and show congruence with the numerical results.

For the validation of damage evolution, the numerical local material behavior is investigated and visualized in Figs. 9–11 for the different directions and failure criteria. The tangential direction is not shown because of its similar behavior to the radial direction. Only a part of the model, representing the region of interest, is shown in these plots. The damaged area of interest is captured at three different time steps in Figs. 9, 11. Damage initiation at σ_{max} in loading direction is shown in the first column followed by damage evolution in the second column, when micro-cracks evolve. And finally, the formation of a macro-crack before failure is shown in the third column, when the first fully damaged elements are deleted. By considering linear elastic and brittle material behavior for tension, once damage is initiated, softening of the material occurs instantly. Therefore, damage develops rapidly within a time frame of 0.5 s, which immediately leads to the failure of the material. Such behavior can be seen in both, experimental and numerical tests. For radial direction slight nonlinear elasticity can be seen in the experiments, which is not covered for the simulations.

Fig. 9 shows the main damage variables in the normal stress directions d_L, d_R, d_T as well as the driving stress σ_{11} for the model loaded in fiber direction with the SDM initiation criterion. For this loading direction, all three damage parameters contribute to damage, whereas in radial or tangential loading direction only the damage variable in loading direction contributes to damage/failure. The reason for this is the stress redistribution due to initial damage and the respectively low strength in the directions perpendicular to the fiber. When damage

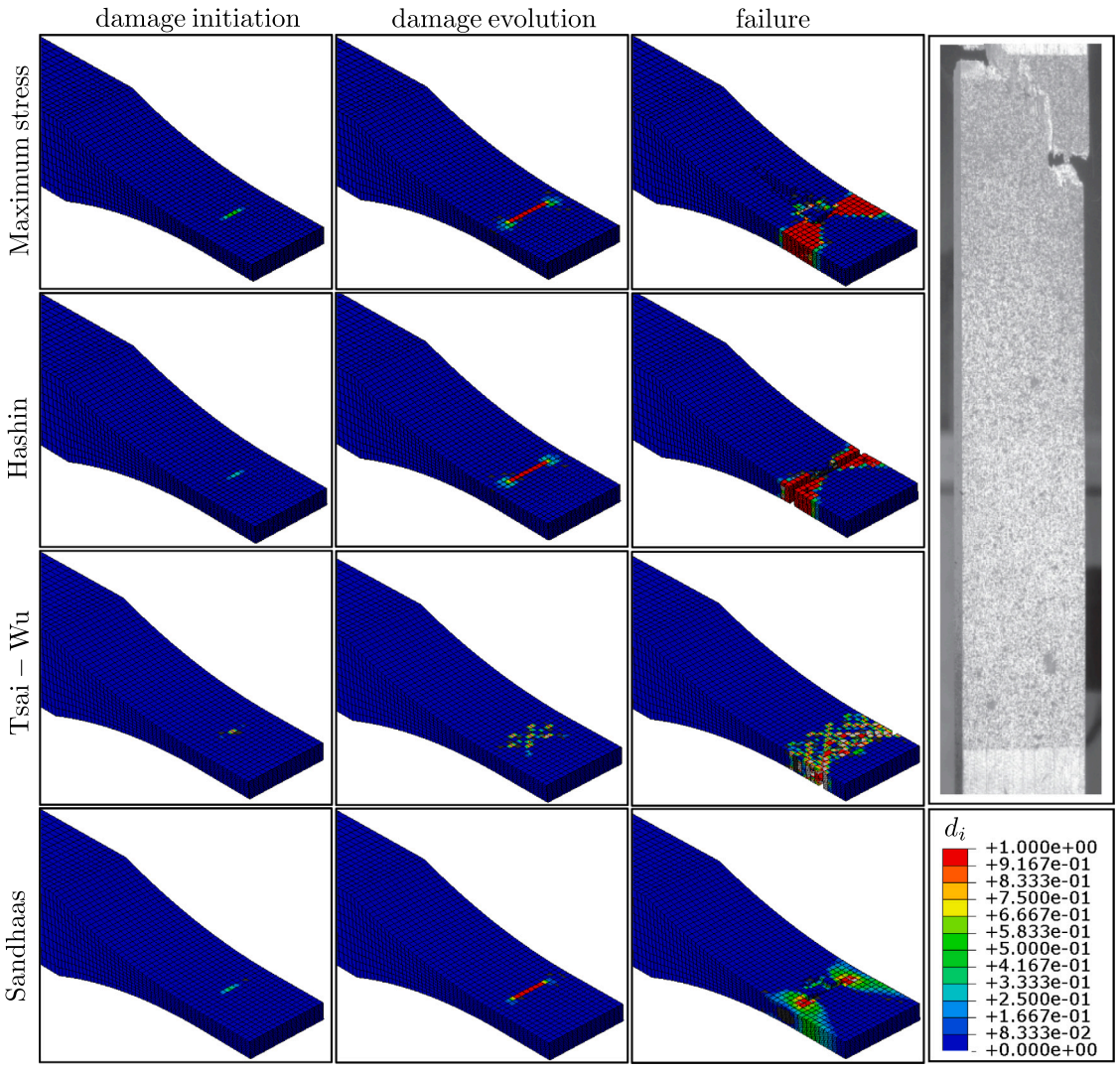

Fig. 10. Numerical progression of the fiber damage variable d_L in longitudinal loading direction for different damage initiation criteria (rows) at different time steps (columns): Damage initiation, damage evolution and failure. The experimental failure mode for a representative sample is shown in the right column.

initiates in fiber direction, the material starts to weaken at the location of maximum stress and consequently the load transfers to undamaged parts. Therefore, damage also initiates in tangential direction and forms the mixed failure mode of tangential and fiber splitting, also shown in the experimental failure crack path in Fig. 9 on the right side. The numerical failure path initiates from the inside and propagates into the lateral direction of the sample (width). In experimental results, this behavior cannot be captured by the camera system due to the abrupt highly brittle behavior. Figs. 10 and 11 show the behavior of different damage initiation criteria. They represent similar damage evolution for all damage initiation criteria in this axial loading case with the exception of Tsai–Wu. The results of the SDM-, Sandhaas- and Hashin-criterion differ slightly due to the considered stress interactions in the latter two criteria. The first two criteria do not combine radial and tangential stresses in one criterion and result thus in different failure modes, visualized in Fig. 10. Tsai–Wu criterion suffers from bifurcation probably due to the mixed compression and tensile strength parameters.

Analogously, the radial direction is visualized in Fig. 11. Similar to the global structural response in direction perpendicular to the fiber, the local damage evolution and the final failure modes are also comparable for all damage initiation criteria.

In conclusion, the focus of this benchmark example is the validation of the damage initiation criteria. Due to axial loading conditions and global fiber orientation, the comparison of damage initiation criteria is performed at a systematically simplified stress situation. Differences among the damage initiation criteria exist and affect the resulting failure mode. Whereas existing failure criteria incorporate the stress interactions by means of summation of stress–strength ratios, the SDM criterion initiates all separated damage variables simultaneously. Once damage initiates in one direction, the second/third direction could still be loaded. Nevertheless, as a consequence of the damage initiation in the first direction, stress redistributions in second/third direction influence immediately the damaged stress state and subsequently result in damage in second/third direction.

Element deletion (as explained in Section 3) is activated to represent discontinuities in a straight-forward solution. Additionally, it needs to be pointed out that, although the crack band method is implemented already in the models, damage is still mesh dependent and the model suffers from localized energy in single elements during damage evolution. As shown in Fig. 10, a very fine mesh is used in this study to

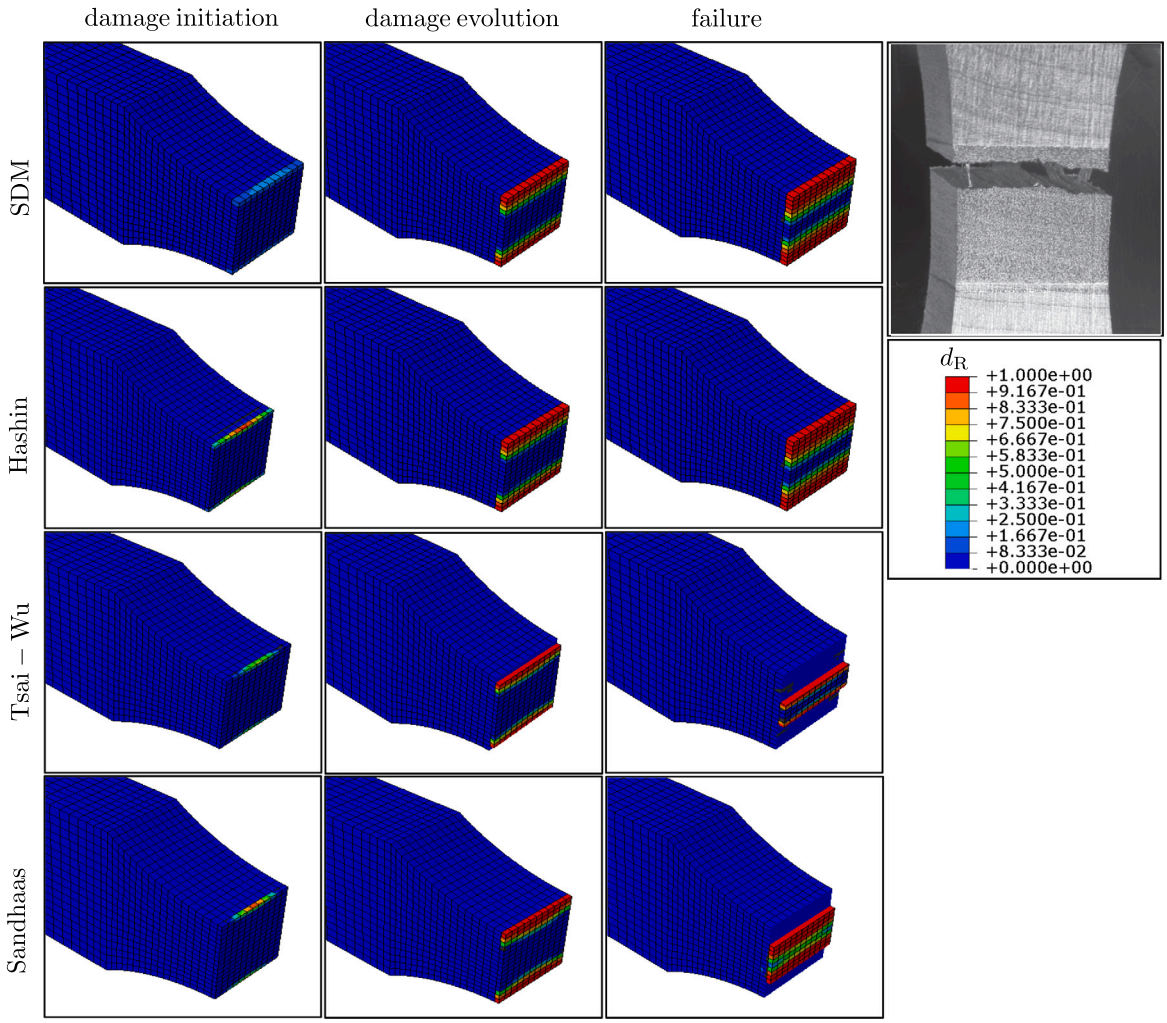

Fig. 11. Numerical progression of the fiber damage variable d_R in radial loading direction for different damage initiation criteria (rows) at different time steps (columns): Damage initiation, damage evolution and failure. The experimental failure mode for a representative sample is shown in the right column.

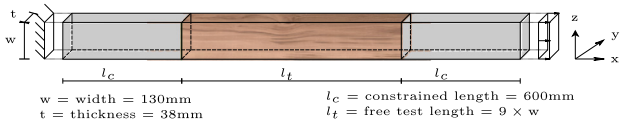

Fig. 12. Tensile test setup with corresponding dimensions according to [7] visualizing the board with fiber deviations.

capture the damage propagation and failure mode resulting in higher computational costs.

4.3. Application example on tensile tested board with local fiber directions

The last example shows the application of the presented elasto-plastic-damage model to a tensile tested sawn beech board with fiber deviations. An exemplary sample from the test set presented in [7], with only local fiber deviation and no strong heterogeneities such as knots, is chosen to increase complexity gradually and validate the mechanical response. The geometrical dimensions and mechanical setup of the experimental tensile test are shown in Fig. 12. Further, the inclusion of local fiber deviation according to laser scanning measurements and its mapping from the real board to the numerical FE model is done according to [7]. In the experimental test, a clamping pressure of 4 MPa is applied on the clamping surfaces before the sample is pulled displacement controlled in x-direction. The same is represented in the numerical model. The boundary conditions are applied in the clamping regions on the wide sides of the board, analogously to the experiment. The displacement DOFs of the four clamped surfaces are constraint to four reference points (RPs) separately to provide rigidity of the contact surfaces and the BCs are then applied on the RPs. In x-direction one side is fixed and on the other side the predefined displacement is applied. In y-direction, one side is fixed and on the other side the clamping pressure is applied. All four surfaces are fixed in z-direction. Two loading steps are separated: Initially, the 4 MPa (according to the experiment) clamping pressure is applied in 10 steps with a linear gradient and kept constant subsequently. Next, a displacement of 3 mm is applied with an increment size of maximum 0.03 mm.

The mesh was adopted to elements with a size of 5 mm in the region of interest (at the boundary conditions and in regions with strong fiber deviation) for satisfying the numerical accuracy with respect to damage and plasticity.

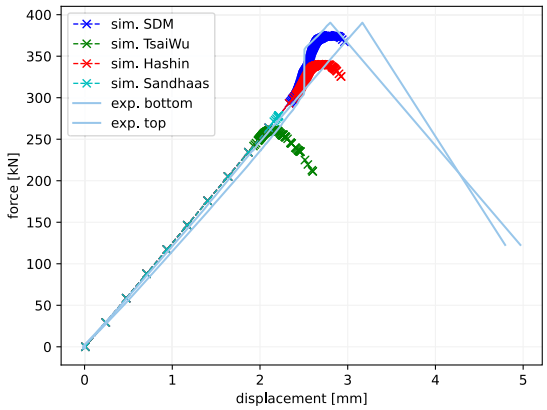

Fig. 13. Experimental and numerical global results of the tensile tested board with fiber deviation for different damage initiation criteria.

4.3.1. Experimental and numerical results

The global structural response of both experimental and numerical tests is visualized in Fig. 13. The light blue curves represent the experimental results from the displacement measured on top and on the bottom of the board. The dotted lines show the different damage initiation criteria. Other than for the dogbone-shaped tensile tests in Section 4.2, a clear difference between the damage initiation criteria is visible. The force–displacement graph in Fig. 13 shows congruent behavior for simulation and experimental results in the elastic range with a stiffening behavior before reaching the maximum force. This stiffening is dependent on the position of displacement measurement within the board: The experimental displacement measured on the bottom of the board (with more distance to the fiber deviation) increases less than the displacement measurement at the top of the board near the fiber deviation. The same stiffening effect is displayed by the simulation (SDM- and Hashin-criterion), where the displacement was measured at the same point like the experimental top edge. Generally, criteria which take stress interactions into account initiate damage at a lower stress state due to the summation of separate stress–strength-ratios presented in Section 2.2. The criterion, which shows the global structural force–displacement response closest to the experiment, is the SDM criterion and accounts for all stresses separately.

Apart from the global structural response, the local damage behavior is visualized in Fig. 14. Already the results in the elastic range of the material, presented in [7], show the development of local stress concentrations due to local fiber deviations in boards loaded in global x-direction. The elasto-plastic damage model presented in this study additionally captures the post-elastic material behavior and can thus predict the initiation of micro-cracks, adding up to a single macro-crack and consequently leading to failure. Comparing each local stress component with its strength, or a combination of stress–strength ratios, initiates the appropriate damage variable. Following the damage evolution law in Eq. (30), the initiated damage variables evolve and weaken the stiffness matrix. Due to the stress concentrations σ_{33} and σ_{13} caused by local fiber deviation, in this case d_T and d_{LT} are initiated simultaneously. Fig. 14 shows two states of the numerical response: On the left side damage initiation at 2.4 mm displacement and on the right side, damage evolution before failure of the whole board at 2.9 mm displacement. Both, the local driving stresses σ_{33}, σ_{13} and its according damage variables d_T, d_{LT} are shown for the SDM criterion. At the same time both damage variables reduce the strength of the material in its according directions. This consequently leads to redistribution of local stresses and represents indirectly stress interactions. Once the first damage parameter reaches the value of one in all eight integration points of an element, the element is being deleted, similar to the opening of a macro-crack. In this way not only stress interactions but

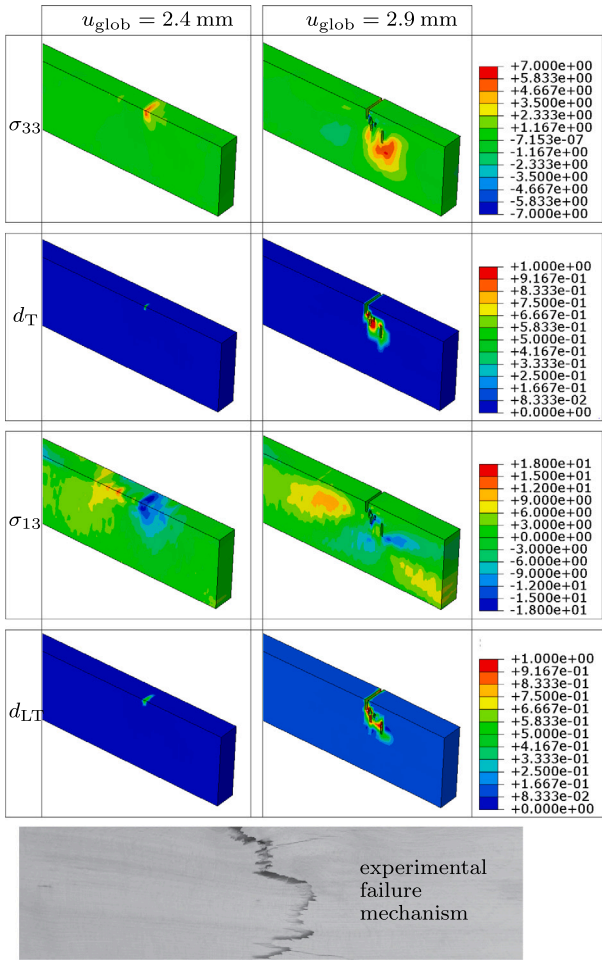

Fig. 14. Driving stress in [MPa] and its corresponding damage variable at damage initiation and damage evolution (before failure) for the SDM criterion besides the experimental failure mechanism.

also the combination of different failure modes in one test sample can be modeled, similar to the frequently observed failure mechanism in tensile/bending tests of sawn timber [41].

In the literature stress–strength-ratios in different directions are summed up either linearly or in a quadratic form for the damage initiation criteria. This aims to represent stress interactions including both normal and shear stresses. Different stress combinations are considered in the four different criteria analyzed in this study: Tsai–Wu, Hashin, Sandhaas and SDM. The specific combinations of stresses are inspired either by fiber composites with transverse isotropic behavior or mainly phenomenologically based on experiments to represent certain failure behavior. Nevertheless, unlike for joint analysis, homogenization and simplification to transverse isotropy is not possible for 3D orthotropic modeling of wood with imperfections. Thus, the representation of stress interactions by means of combination and summation in the damage initiation criterion leads to early failure and might be replaced by SDM criterion. In the latter criterion, damage weakens the material locally and separately for all directions, but consequently leads to stress redistributions and damage in other directions. Considering separate damage variables for different stresses at the same time cannot only be seen as a different interpretation of stress interactions but is also representing the orthotropic behavior consistently and thus allows a better differentiation between failure modes. Consequently, it is pointed out that stress transformation due to local fiber deviations together with damage initiation criteria that take stress interactions in form of stress summation into account, may predict damage and failure to occur at

earlier stress-states. A remaining challenge for this model is the strong mesh dependency and convergence at the stage of damage evolution.

5. Conclusion

This study approaches to capture the post-elastic material behavior numerically, which is necessary to improve the strength prediction of e.g. beech lamellas for optimized GLT.

Fundamental for such a numerical representation is an elasto-plastic damaging material model incorporating the three-dimensional behavior of this heterogeneous material as well as experimental validation in all directions.

In consideration of existing transversely isotropic elasto-plastic damaging material models from the state of the art, the material model in this contribution was enhanced for full orthotropy. On one side, this implied the focus on the post-elastic behavior: In compression, the Hill48-plasticity criterion with nonlinear hardening was enhanced for incorporation of the crucial loading direction. A systematic experimental testing of clear wood samples provided the crucial strain results for validation in three dimensions.

On the other side in tension, different damage initiation criteria were analyzed and validated on clear wood dogbone-shaped samples axially loaded in tension in all three orthotropic directions. Interactive damage criteria, combining different stress directions, were further compared for the three-dimensional damage effect in sawn boards with fiber deviation. In such cases homogenization and simplification to transverse isotropy was not possible due to the fiber deviations. Local fiber directions needed to be accounted and damage initiation was modeled most accurately by means of separated damage variables. Conversely, the summation of the stresses in combined criteria resulted in an underestimation of the failure behavior. Further, it was shown in this study that for the case of an orthotropic and heterogeneous material, experimental results could be captured well numerically. With different damage variables evolving simultaneously, cracks were modeled. The consequence were stress redistributions and subsequently accumulating to a macro-crack, resulting in specific types of failure modes for wood.

The detailed incorporation of shear failure behavior to the plasticity criterion will be an important step for the future, while considering the whole 3D orthotropic stress situation. Despite including the crack band method, a further remaining challenge for the model is the mesh dependency and convergence at the stage of damage evolution. This illustrates one outlook of the future work, where other regularization approaches for the representation of the fracture may be considered and incorporated into the model. Further, a systematic validation of loaded boards with strong heterogeneities such as strong fiber deviations including knots need to be analyzed carefully including detailed experimental validation with local strain measurement.

CRediT authorship contribution statement

Franziska Seeber: Writing – review & editing, Writing – original draft, Visualization, Validation, Software, Methodology, Investigation, Formal analysis, Data curation, Conceptualization. **Ani Khaloian-Sarnaghi:** Writing – review & editing, Supervision, Project administration, Methodology, Funding acquisition, Conceptualization. **Taoyi Yu:** Writing – review & editing, Methodology, Formal analysis. **Fabian Duddeck:** Writing – review & editing, Supervision, Conceptualization. **Jan-Willem van de Kuilen:** Writing – review & editing, Supervision, Resources, Funding acquisition, Conceptualization.

Declaration of competing interest

We wish to confirm that there are no known conflicts of interest associated with the publication "Development and validation of an orthotropic 3D elasto-plastic damage model for wood considering heterogeneities and anisotropy". We further confirm that the manuscript has been read and approved by all named authors and that there are no other persons who satisfied the criteria for authorship but are not listed. The order of authors is listed in the manuscript and has been approved by all of us. We confirm that this manuscript is original, has not been published before and is not currently being considered for publication elsewhere. We understand that the Corresponding Author is the sole contact for the Editorial process. He/she is responsible for communicating with the other authors about progress, submissions of revisions and final approval of proofs.

Data availability

The data that has been used is confidential.

Acknowledgments

Supported by TUM International Graduate School of Science and Engineering (IGSSE).

The authors thank HoMaba project supported by "Fachagentur Nachwachsende Rohstoffe e.V. (FNR)" on behalf of BMEL under the grant number 22002918 for the experimental data used in this study.

Appendix A. Nomenclature

$\boldsymbol{\sigma}$	stress tensor
$\hat{\boldsymbol{\sigma}}$	effective stress tensor
$\boldsymbol{\varepsilon}^{\mathrm{e}}$	elastic strain tensor
$\boldsymbol{\varepsilon}^{\mathrm{p}}$	plastic strain tensor
$\mathbf{C}_0$	initial undamaged orthotropic stiffness tensor
$\mathbf{C}_{\mathrm{d}}$	damaged orthotropic stiffness tensor
$\mathbf{C}_{\mathrm{ep}}$	elastic–plastic stiffness tensor
$\mathbf{D}_{\mathrm{d}}$	damaged compliance matrix
$\mathbf{A}$	matrix of material parameters for Hill (1948)
$\tilde{\mathbf{A}}$	matrix of material parameters for adapted Hill (1948)
i	$= [L, R, T]$; direction regarding the fiber orientation: longitudinal (L), radial (R), tangential (T)
E_i	stiffness modulus
ν_{ij}	Poisson's ratio
G_{ij}	shear modulus
$f_{\mathrm{y},i}$	yield strength
$f_{\mathrm{c},i}$	ultimate compressive strength
$f_{\mathrm{t},i}$	tensile strength
$f_{\mathrm{v},ij}$	shear strength
q_i	hardening law
Q_i	hardening modulus
b_i	hardening model parameter
α_i	hardening variable
$\Delta\lambda$	plastic consistency parameter
F_i	ith failure function
ϕ_i	ith limit state function
κ_i	ith state variable
$d_{\mathrm{t/v},i}$	tensile damage variable
$d_{\mathrm{c},i}$	compression damage variable
$\mathrm{g}_{\mathrm{f},i}$	regularized fracture energy
h	characteristic element length
$\mathrm{G}_{\mathrm{f},i}$	fracture energy
$\mathrm{G}_{\mathrm{f,v}}$	longitudinal shear fracture energy
$\mathrm{G}_{\mathrm{f,roll}}$	rolling shear fracture energy
η	fictitious viscosity parameter
GAU	Georg-Augustin-Universität Göttingen
THR	Technische Hochschule Rosenheim

Appendix B. Elasto-plastic damage model - Algorithmic solution

Following [30], in the initialization step the current effective stress and plastic strain are determined and the plastic strain hardening variable is initialized as:

$$\begin{aligned}
\boldsymbol{\varepsilon}^{p}_{n+1} &= \boldsymbol{\varepsilon}^{p}_{n} + \Delta\lambda \frac{\partial f}{\partial \boldsymbol{\sigma}_{n+1}},\\
\alpha_{n+1} &= \alpha_n + \Delta\lambda \frac{\partial f}{\partial q_{n+1}},\\
\hat{\boldsymbol{\sigma}}_{n+1} &= \mathbf{C}_0 : (\boldsymbol{\varepsilon}_{n+1} - \boldsymbol{\varepsilon}^{p}_{n+1}),\\
f_{n+1} &= f(\boldsymbol{\sigma}_{n+1}, \alpha_{n+1}) = 0.
\end{aligned} \tag{34}$$

The failure criterion f is now used to check whether the current stress state is inside, outside, or on the yield surface. If f is less than zero, we are in the elastic stress state, which requires no further adjustments to the stiffness matrix. If this is not the case, the current effective elastic predictor stress is calculated:

$$\hat{\boldsymbol{\sigma}}^{\text{trial}}_{n+1} = \hat{\boldsymbol{\sigma}}_n + \mathbf{C}_0 : \Delta\boldsymbol{\varepsilon}, \tag{35}$$

and the plastic corrector needs to be calculated iteratively with the numerator of iterations k (all variables have the subscript k which is submitted in the following equations):

$$\begin{aligned}
\hat{\boldsymbol{\sigma}}_{n+1} &= \hat{\boldsymbol{\sigma}}_n + \mathbf{C}_0 : \Delta\boldsymbol{\varepsilon}^{e} = \hat{\boldsymbol{\sigma}}_n + \mathbf{C}_0(\Delta\boldsymbol{\varepsilon} - \Delta\boldsymbol{\varepsilon}^{p})\\
&= \hat{\boldsymbol{\sigma}}^{\text{trial}}_{n+1} - \mathbf{C}_0 : \Delta\boldsymbol{\varepsilon}^{p}.
\end{aligned} \tag{36}$$

On the basis of the plastic strain increment

$$\Delta\boldsymbol{\varepsilon}^{p}_{n+1} = \mathbf{D}_0 : (\hat{\boldsymbol{\sigma}}^{\text{trial}}_{n+1} - \hat{\boldsymbol{\sigma}}_{n+1}), \tag{37}$$

the plastic flow residuals are calculated, which need to converge to 0 during the iterations:

1. Plastic strain residual as

$$\mathbf{r}^{\boldsymbol{\varepsilon}^p}_{n+1} = \mathbf{D}_0 : (\hat{\boldsymbol{\sigma}}_{n+1} - \hat{\boldsymbol{\sigma}}^{\text{trial}}_{n+1}) + \Delta\lambda_{n+1} \frac{\partial f}{\partial \hat{\boldsymbol{\sigma}}_{n+1}} = 0. \tag{38}$$

2. Equivalent plastic strain residual (or residual of the plastic hardening variable) as

$$\mathrm{r}^{\alpha}_{n+1} = -\alpha_{n+1} + \alpha_n + \Delta\lambda_{n+1} \frac{\partial f}{\partial q}. \tag{39}$$

3.Failure surface as

$$f_{n+1} = f_{n+1}(\hat{\boldsymbol{\sigma}}_{n+1}, \alpha_{n+1}). \tag{40}$$

Considering the hardening law, the growth of the consistency parameter is determined with linearization:

$$\begin{aligned}
\mathbf{r}^{\boldsymbol{\varepsilon}^p}_{n+1} + \mathbf{D}_0 : \delta\hat{\boldsymbol{\sigma}}_{n+1} + \delta\Delta\lambda_{n+1} \frac{\partial f}{\partial \hat{\boldsymbol{\sigma}}_{n+1}} + \Delta\lambda_{n+1} \frac{\partial^2 f}{\partial \hat{\boldsymbol{\sigma}}^2_{n+1}} \delta\hat{\boldsymbol{\sigma}}_{n+1} = 0,\\
\mathrm{r}^{\alpha}_{n+1} - \delta\alpha_{n+1} + \delta\Delta\lambda_{n+1} \frac{\partial^2 f}{\partial q^2} = 0,\\
f_{n+1} + \frac{\partial f}{\partial \hat{\boldsymbol{\sigma}}_{n+1}} \delta\hat{\boldsymbol{\sigma}}_{n+1} + \frac{\partial f}{\partial q} \frac{\partial q}{\partial \alpha} \delta\alpha_{n+1} = 0,
\end{aligned} \tag{41}$$

reformulation:

$$\begin{aligned}
\delta\hat{\boldsymbol{\sigma}}_{n+1} &= \frac{\mathbf{r}^{\boldsymbol{\varepsilon}^p}_{n+1} + \delta\Delta\lambda_{n+1} \dfrac{\partial f}{\partial \hat{\boldsymbol{\sigma}}_{n+1}}}{-\left(\mathbf{D}_0 + \Delta\lambda_{n+1} \dfrac{\partial^2 f}{\partial \hat{\boldsymbol{\sigma}}^2_{n+1}}\right)},\\
&= -\left(\mathbf{r}^{\boldsymbol{\varepsilon}^p}_{n+1} + \delta\Delta\lambda_{n+1} \frac{\partial f}{\partial \hat{\boldsymbol{\sigma}}_{n+1}}\right)\mathbf{C}^{-1}_{n+1},\\
\delta\alpha_{n+1} &= \mathrm{r}^{\alpha}_{n+1} + \delta\Delta\lambda_{n+1} \frac{\partial^2 f}{\partial q^2_{n+1}},\\
\text{with}\quad \mathbf{C}_{n+1} &= \left(\mathbf{D}_0 + \Delta\lambda_{n+1} \frac{\partial^2 f}{\partial \hat{\boldsymbol{\sigma}}^2_{n+1}}\right)^{-1},
\end{aligned} \tag{42}$$

and substitution:

$$\delta\Delta\lambda_{n+1} = \frac{f_{n+1} + \dfrac{\partial f}{\partial \hat{\boldsymbol{\sigma}}_{n+1}}(-\mathbf{C}_{n+1})\mathbf{r}^{\boldsymbol{\varepsilon}^p}_{n+1} + \dfrac{\partial f}{\partial q}\mathrm{r}^{\alpha}_{n+1}}{\dfrac{\partial f}{\partial \hat{\boldsymbol{\sigma}}_{n+1}} : \mathbf{C}_{n+1} : \dfrac{\partial f}{\partial \hat{\boldsymbol{\sigma}}_{n+1}} - \dfrac{\partial f}{\partial q_{n+1}} \dfrac{\partial^2 f}{\partial q^2_{n+1}}}. \tag{43}$$

Consequently the increase in plastic strains and internal variables results in the following update of internal variables:

$$\begin{aligned}
\hat{\boldsymbol{\sigma}}^{(k+1)}_{n+1} &= \hat{\boldsymbol{\sigma}}^{(k)}_{n+1} + \delta(\hat{\boldsymbol{\sigma}}_{n+1})^{(k)},\\
\boldsymbol{\varepsilon}^{p(k+1)}_{n+1} &= \boldsymbol{\varepsilon}^{p(k)}_{n+1} - \mathbf{D}_0 : (\delta\hat{\boldsymbol{\sigma}}_{n+1})^{(k)},\\
\boldsymbol{\varepsilon}^{e(k+1)}_{n+1} &= \boldsymbol{\varepsilon}^{(k+1)}_{n+1} - \boldsymbol{\varepsilon}^{p(k+1)}_{n+1},\\
\alpha^{(k+1)}_{n+1} &= \alpha^{(k)}_{n+1} + \delta\alpha^{(k)}_{n+1},\\
\Delta\lambda^{(k+1)}_{n+1} &= \Delta\lambda^{(k)}_{n+1} + \delta\Delta\lambda^{(k)}_{n+1}.
\end{aligned} \tag{44}$$

The local iteration is considered to be finished as soon as both the yield surface and the residua are less than or equal to the given tolerance of 1×10^{-6} to ensure acceptable accuracy of the solution as well as limited calculation time. Once the local iteration is finished, the elastic–plastic tangent stiffness matrix is determined:

$$\mathbf{C}_{\text{ep}} = \mathbf{C}_{n+1} - \frac{\mathbf{C}_{n+1} : \dfrac{\partial f}{\partial \hat{\boldsymbol{\sigma}}_{n+1}} \otimes \dfrac{\partial f}{\partial \hat{\boldsymbol{\sigma}}_{n+1}}}{\dfrac{\partial f}{\partial \hat{\boldsymbol{\sigma}}_{n+1}} : \mathbf{C}_{n+1} : \dfrac{\partial f}{\partial \hat{\boldsymbol{\sigma}}_{n+1}} + \dfrac{\partial f}{\partial q_{n+1}} \dfrac{\partial q}{\partial \alpha}}. \tag{45}$$

In the next step, damage yield functions ϕ_i according to Section 2.2 are checked and damage variables d_i are calculated. The damaged compliance $\mathbf{D}_{\text{d}}$ and the damaged stiffness matrix $\mathbf{C}_{\text{d}}$ can now be calculated according to Eq. (33). Following CDM and Hook's law the stress tensor is updated according to

$$\boldsymbol{\sigma} = \mathbf{C}_{\text{d}}\boldsymbol{\varepsilon}^{\text{e}}. \tag{46}$$

Further, also the tangent stiffness matrix needs to be adapted according to the next steps: The crack band method is considered for regularization, where the fracture energy is expressed by means of the characteristic element length h:

$$g_{\text{f},i} = \frac{\mathrm{G}_{\text{f},i}}{h}. \tag{47}$$

To improve the convergence of the material model, a fictitious viscous parameter η is introduced, which leads to a remaining positive definite stiffness matrix and thus a more robust solution process with less convergence problems. The rate of the stabilized damage variable d^{v}_{i} is calculated to

$$\dot{d}^{v}_{i} = \frac{(d_i - d^{v}_{i})}{\eta}, \tag{48}$$

and can be discretized in fictitious time leading to the damage variable with t being the fictitious time increment

$$d^{v}_{n+1} = \max\left\{0, d^{v,t-1}, \frac{\eta}{\eta + \Delta t} d^{v}_{n} + \frac{\Delta t}{\eta + \Delta t} d_{n+1}\right\}. \tag{49}$$

This further guarantees the irreversibility of the damage process. Finally the Jacobian matrix needs to be adjusted according to damage and the consistent tangential stiffness matrix in accordance with [30] by differentiating the stress in Eq. (46):

$$\begin{aligned}
\mathrm{d}\boldsymbol{\sigma} &= \left[\frac{\partial \mathbf{C}_{d^v}}{\partial \boldsymbol{\varepsilon}^{e}} : \boldsymbol{\varepsilon}^{e} + \mathbf{C}_{\mathrm{d}^v}\right]\mathrm{d}\boldsymbol{\varepsilon}^{e},\\
\mathrm{d}\boldsymbol{\sigma} &= \left[\frac{\partial \mathbf{C}_{d^v}}{\partial \boldsymbol{\varepsilon}^{e}} : \boldsymbol{\varepsilon}^{e} + \mathbf{C}_{d^v}\right] : \mathbf{C}^{-1}_{0} : \mathrm{d}\hat{\boldsymbol{\sigma}},\\
\mathrm{d}\hat{\boldsymbol{\sigma}} &= \mathbf{C}_{\text{ep}} : \mathrm{d}\boldsymbol{\varepsilon},\\
\frac{\partial \boldsymbol{\sigma}}{\partial \boldsymbol{\varepsilon}} &= \left[\frac{\mathbf{C}_{d^v}}{\partial \boldsymbol{\varepsilon}^{e}} : \boldsymbol{\varepsilon}^{e} + \mathbf{C}_{d^v}\right] : \mathbf{C}^{-1}_{0} : \mathbf{C}_{\text{ep}},
\end{aligned} \tag{50}$$

$$\frac{\partial \boldsymbol{\sigma}}{\partial \boldsymbol{\varepsilon}} = \left\{ \mathbf{C}_{d_{n+1}^v} + \sum_{i=1}^{n} \left(\frac{\partial \mathbf{C}_{d^v}}{\partial d_i^v} : \boldsymbol{\varepsilon}^e \right) \times \left(\frac{\partial d_i^v}{\partial d_i} \frac{\partial d_i}{\partial f_i} \frac{\partial f_i}{\partial \boldsymbol{\varepsilon}^e} \right) \Big|_{n+1} \right\} : \mathbf{C}_0^{-1} : \mathbf{C}_{\text{ep}}. \tag{51}$$

References

[1] Frühwald K, Schickhofer G. Strength grading of hardwoods. In: 8th World Conference on Timber Engineering. 2004, p. 675–9, WCTE 2004.

[2] Westermayr M, Stapel P, van de Kuilen J-W. Tensile and Compression Strength of Small Cross Section Beech (*Fagus S.*) Glulam Members. In: INTER proceedings. 2018.

[3] Bader TK, Omarsson S. Modeling the mechanical behavior of wood materials and timber structures. In: Springer Handbook of Wood Science and Technology. Springer; 2023, p. 507–68.

[4] Lukacevic M, Kandler G, Hu M, Olsson A, Füssl J. A 3D model for knots and related fiber deviations in sawn timber for prediction of mechanical properties of boards. Mater Des 2019;166:107617.

[5] Khaloian Sarnaghi A, van de Kuilen J-W. An advanced virtual grading method for wood based on surface information of knots. Wood Sci Technol 2019;53(3):535–57.

[6] Hu M. Studies of the fibre direction and local bending stiffness of Norway spruce timber: for application on machine strength grading [Dissertation], Växjö: Linnaeus University; 2018.

[7] Seeber F, Khaloian A, Rais A, van de Kuilen JW. A numerical strength prediction approach for wood using elementwise local fiber directions from laser scanning. Mater Des 2023;226:111578.

[8] Huber JA, Broman O, Oja J, Ekevad M. Generating 3D finite element models of boards from computer tomography images. In: ECCOMAS Congress. 2020.

[9] Hill R. A theory of the yielding and plastic flow of anisotropic metals. Proc R Soc Lond Ser A Math Phys Sci 1948;193(1033):281–97.

[10] Tsai SW, Wu EM. A general theory of strength for anisotropic materials. J Compos Mater 1971;5(1):58–80.

[11] Mackenzie-Helnwein P, Eberhardsteiner J, Mang HA. A multi-surface plasticity model for clear wood and its application to the finite element analysis of structural details. Comput Mech 2003;31(1–2):204–18.

[12] Schmidt J, Kaliske M. Zur dreidimensionalen Materialmodellierung von Fichtenholz mittels eines Mehrflächen-Plastizitätsmodells. Holz als Roh- und Werkstoff 2006;64(5):393–402.

[13] Schmidt J, Kaliske M. Simulation of cracks in wood using a coupled material model for interface elements. Holzforschung 2007;61(4):382–9.

[14] Lemaître J, Desmorat R. Engineering damage mechanics: ductile, creep, fatigue and brittle failures. Springer Science & Business Media; 2005.

[15] Maimí P, Camanho PP, Mayugo JA, Dávila CG. A continuum damage model for composite laminates: Part I – constitutive model. Mech Mater 2007;39(10):897–908.

[16] Matzenmiller A, Lubliner J, Taylor RL. A constitutive model for anisotropic damage in fiber-composites. Mech Mater 1995;20(2):125–52.

[17] Sandhaas C. Mechanical behaviour of timber joints with slotted-in steel plates [Dissertation], Delft: Technische Universitet Delft; 2012.

[18] Norris CB. Strength of orthotropic materials subjected to combined stresses. Forest Products Laboratory, Forest Service, U.S. Department of Agriculture; 1962.

[19] Hashin Z. Failure criteria for unidirectional fiber composites. J Appl Mech 1980;47(4):329–34.

[20] Mascia NT, Simoni RA. Analysis of failure criteria applied to wood. Eng Fail Anal 2013;35:703–12.

[21] Schmidt J, Kaliske M. Models for numerical failure analysis of wooden structures. Eng Struct 2009;31(2):571–9.

[22] Lukacevic M, Lederer W, Füssl J. A microstructure-based multisurface failure criterion for the description of brittle and ductile failure mechanisms of clear-wood. Eng Fract Mech 2017;176:83–99.

[23] Benvenuti E, Orlando N, Gebhardt C, Kaliske M. An orthotropic multi-surface damage-plasticity FE-formulation for wood: Part II – numerical applications. Comput Struct 2020;240.

[24] Pech S, Lukacevic M, Füssl J. Simulation of wood fracture mechanics using the phase field method for fracture. In: 13th World Conference on Timber Engineering. 2023, p. 391–7, WCTE 2023.

[25] Karimi-Nobandegani A, Gharib M, Valipour H. A nonlocal continuum damage model for timber: Development, implementation, and application. Eng Fract Mech 2023;277:109009.

[26] Serrano E. Adhesive joints in timber engineering - modelling and testing of fracture porperties [Doctoral thesis], Lund: Lund University; 2000.

[27] Franke B, Quenneville P. Numerical modeling of the failure behavior of dowel connections in wood. J Eng Mech 2011;137(3):186–95.

[28] van der Linden MLR, van de Kuilen J-W, Blass HJ. Application of the Hoffman yield criterion for load sharing in timber sheet pile walls. In: Pacific timber engineering conference. Gold Coast, Australia; 1994, p. 412–7.

[29] Gharib M, Hassanieh A, Valipour H, Bradford MA. Three-dimensional constitutive modelling of arbitrarily orientated timber based on continuum damage mechanics. Finite Elem Anal Des 2017;135:79–90.

[30] Wang M, Song X, Gu X. Three-dimensional combined elastic–plastic and damage model for nonlinear analysis of wood. J Struct Eng 2018;144(8):04018103.

[31] Zhang L, Xie Q, Zhang B, Wang L, Yao J. Three-dimensional elastic–plastic damage constitutive model of wood. Holzforschung 2020;75(09).

[32] Benvenuti E, Orlando N, Gebhardt C, Kaliske M. An orthotropic multi-surface damage-plasticity FE-formulation for wood: Part I – constitutive model. Comput Struct 2020;240.

[33] Eberhardsteiner J. Mechanisches Verhalten von Fichtenholz: Experimentelle Bestimmung der biaxialen Festigkeitseigenschaften. Springer Vienna; 2002.

[34] Akter ST, Serrano E, Bader TK. Experimental assessment of failure criteria for the interaction of normal stress perpendicular to the grain with rolling shear stress in norway spruce clear wood. Eur J Wood Wood Prod 2020;78:1105–23.

[35] van der Put TACM. A general failure criterion for wood. Report, Delft: Technische Universitet Delft; 1982.

[36] Steiger R, Gehri E. Interaction of shear stresses and stresses perpendicular to the grain, paper 44-6-2. In: CIB-w18 meeting 44. Alghero, Italy; 2011.

[37] nan de Kuilen J-W, Gard W, Ravenhorst G, Antonelli V, Kovryga A. Shear strength values for soft-and hardwoods. In: INTER meeting 50. Kyoto, Japan; 2017, p. 49–63.

[38] Akter ST, Serrano E, Bader TK. Numerical modelling of wood under combined loading of compression perpendicular to the grain and rolling shear. Eng Struct 2021;244:112800.

[39] Gibson LJ, Ashby MF. Cellular solids: Structure and properties. In: Cambridge solid state science series, Cambridge University Press; 1997.

[40] Niemz P, Sonderegger WU. Holzphysik: Physik des Holzes und der Holzwerkstoffe. München: Fachbuchverlag Leipzig im Carl Hanser Verlag; 2017.

[41] Bodig J, Jayne BA. Mechanics of wood and wood composites. Krieger Publishing Company: 978-0442008222; 1982, Reprint Edition (1993).

[42] Simo JC, Ju JW. Strain- and stress-based continuum damage models—I. formulation. Math Comput Modelling 1989;12(3):378.

[43] Voce E. The relationship between stress and strain for homogeneous deformation. J Inst Metals 1948;74:537–62.

[44] Simo JC, Hughes TJR. Computational inelasticity. Vol. 7, Springer Science & Business Media; 2006.

[45] Bažant ZP, Oh BH. Crack band theory for fracture of concrete. Matériaux et Constructions 1983;16(3):155–77.

[46] Ozyhar T, Hering S, Niemz P. Moisture-dependent elastic and strength anisotropy of European beech wood in tension. J Mater Sci 2012;47:6141–50.

[47] Bucur V. Acoustics of wood. In: Springer Series in Wood Science. Springer; 2006.

[48] Bollmus S, Buchelt B, Deetz R, Eichhorn S, Engelhardt M, Gecks J, et al. Schlussbericht Verbundvorhaben: Holzbasierte Werkstoffe im Maschinenbau (HoMaba) – Berechnungskonzepte, Kennwertanforderungen, Kennwertermittlung, Vol. 12, 2022.